

Quantum Neural Networks in Practice: A Comparative Study with Classical Models from Standard Data Sets to Industrial Images

Daniel Basilewitsch¹, João F. Bravo^{2,*}, Christian Tutschku² and Frederick Struckmeier¹

¹*Quantum Applications Group, TRUMPF SE + Co. KG,
Johann-Maus-Straße 2, 71254 Ditzingen, Germany*

²*Fraunhofer IAO, Nobelstraße 12, 70569 Stuttgart, Germany*

(Dated: November 18, 2025)

In this study, we compare the performance of randomized classical and quantum neural networks (NNs) as well as classical and quantum-classical hybrid convolutional neural networks (CNNs) for the task of supervised binary image classification. We keep the employed quantum circuits compatible with near-term quantum devices and use two distinct methodologies: applying randomized NNs on dimensionality-reduced data, and applying CNNs to full image data. We evaluate these approaches on three fully-classical data sets of increasing complexity: an artificial hypercube data set, MNIST handwritten digits and industrial images of practical relevance. Our study’s central goal is to shed more light on how quantum and classical models perform for various binary classification tasks and on what defines a good quantum model. To this end, our study involves a correlation analysis between classification accuracy and quantum model hyperparameters, and an analysis on the role of entanglement in quantum models, as well as on the impact of initial training parameters. We find classical and quantum-classical hybrid models achieve statistically-equivalent classification accuracies across most data sets with no approach consistently outperforming the other. Interestingly, we observe that quantum NNs show lower variance with respect to initial training parameters and that the role of entanglement is nuanced. While incorporating entangling gates seems to be generally advantageous, we also observe that their (optimizable) entangling power is not correlated with model performance. We also observe an inverse proportionality between the number of entangling gates and the average gate entangling power. Our study provides an industry perspective on quantum machine learning for practical binary image classification tasks, highlighting both current limitations and potential avenues for further research in quantum circuit design, entanglement utilization, and model transferability across varied applications.

Keywords Quantum neural networks · Hybrid convolutional neural networks · Image classification · Industry benchmark

I. INTRODUCTION

Quantum machine learning [1, 2] is one of the various subfields of quantum computing promising advantages over its classical counterpart, for instance due to proposals regarding more efficient data encoding [3, 4], improved model expressivity [5–7], prediction accuracy [8–10] or by saving computational resources [11]. These theoretical proposals have been backed up by claims of experimental quantum advantage in learning tasks [12, 13]. While these works illustrate the various hopes associated with quantum machine learning, they often rely on very specific assumptions about the problem [10, 11], the availability of quantum data [9, 12–14], or require quantum devices beyond the near-term regime [3, 4]. While there has been undeniable progress in the field of quantum machine learning — both on the algorithmic as well as on the hardware side — doubts about the field’s focus on quantum advantage have been previously raised [15]. Ultimately, this culminated in a recent work questioning the significance of quantum-machine-learning benchmark studies [16], given their predominant use of overly simple

data sets paired with insufficiently-performing quantum hardware. Other works [17–19] even suggest that much of what was commonly believed to be classically hard or intractable to simulate might be efficiently simulable on classical hardware after all. While this raises the question what “quantum” means for quantum machine learning, both Refs. [16, 17] independently call for more rigorous benchmarks employing less trivial data sets in order to assess the potential of quantum machine learning.

In response to this critical need, our work directly addresses this challenge by employing not only standard benchmark data sets, but crucially incorporating industrial data of practical relevance that represents machine-learning applications beyond academic test cases. To put our work into perspective, as pointed out earlier, many papers about (theoretical) quantum advantage require either very specific problem assumptions or quantum data. However, many machine-learning problems of practical relevance have neither very specific problem assumptions, nor quantum data. In the following, we therefore take an industrial perspective on quantum machine learning and want to investigate whether quantum models provide some kind of “practical advantage” for a supervised binary classification task on classical data, compared to classical models. We thereby measure “practical advantage”

* joao.bravo@iao.fraunhofer.de

by the achievable classification accuracies and compare them between classical and quantum models. Since we believe that a fair comparison requires testing of various models and scenarios, we conceive our study as a larger benchmarking study that sheds light on the differences and properties of classical and quantum models and on what defines a good quantum model. We therefore deliver a robust benchmark study in the spirit of Refs. [16, 17], using non-trivial data sets of practical relevance for the industry, while, at the same time, answering the question of how quantum machine learning models of small to near-term scale perform for such a task. We believe this study provides important insights towards auspicious future research directions.

In more detail, we benchmark the performance of classical and quantum-machine-learning models in classifying three classical data sets of increasing data complexity. The data sets include (i) an artificial data set based on linearly splitting a (hyper-)cube in two, (ii) MNIST’s handwritten digits [20] as an easy but well-studied data set and (iii) images from laser cutting machines as a challenging data set from the industry. Note that we use the first two data sets merely as a means to benchmark and validate our employed methodologies, since — as mentioned in Refs. [16, 18] — the potential insights about the power and usefulness of quantum machine learning that can be drawn from simple data sets are very limited. However, we still believe them to be useful for validating the results we obtain for the practically-relevant industrial data set on which we put the main focus when drawing conclusions on quantum machine learning from an industry perspective. Moreover, since we are also interested in testing the cross-data-set performance, assessed by the classification accuracy, of some quantum models, we deem it beneficial to have results for various data sets with different levels of complexity available.

In terms of methodologies, we employ both classical and quantum neural networks [5] as well as classical and quantum-classical hybrid convolutional neural networks [21] to classify any of the mentioned data sets. The dual-methodology approach used allows us to systematically analyze not just the relative performance of classical versus quantum models, but also to extract insights on which quantum architecture aspects contribute most to performance, how hyperparameters correlate with classification accuracy, and whether successful quantum models on one data set transfer well to others — providing a comprehensive framework for quantum advantage assessment in realistic settings. Our decision for parametrized quantum circuits is motivated by their high expressivity [5] which is amplified by techniques like data re-uploading [22, 23] and trainable data embeddings [24] while at the same time keeping quantum hardware requirements moderate. This is in contrast to some early suggestions for quantum-machine-learning models based on amplitude encoding [3, 4, 25], which, despite being qubit-efficient, were later deemed too resource-demanding to run on any near-term device due to their excessive need

of quantum gates for accurate state preparation [6]. In contrast to these advantages, parametrized quantum circuits suffer from barren plateaus [26], which prevents their efficient training at scale, although much work has been put into mitigating or avoiding them, see e.g. Refs. [27–30] to name but a few. Some quantum models, such as quantum convolutional neural networks [31], provably avoid barren plateaus [32] but are classically efficiently simulable [18]. Unfortunately, the latter are also rather resource-demanding to qualify for near-term applicability and practical simulability within this study, which is why we resort to quantum-classical hybrid convolutional neural networks [21] instead. Conceptually, parametrized quantum circuits as well as quantum-classical hybrid convolutional neural networks belong to the realm of variational quantum algorithms [33], where the execution of quantum circuits is carried out on actual quantum hardware, while the calculation of iteratively-updated circuit parameters is performed on classical computers. Due to these choices, our study reflects a current perspective on what quantum-machine-learning methods, suitable for near-term quantum devices, offer for classifying industry-level image data.

The remainder of this paper is structured as follows. In Sec. II we introduce the three different data sets in more detail, before Sec. III presents the main methodological framework based on random neural networks and convolutional neural networks. The results based on the former are shown in Sec. IV, while Sec. V subsequently presents the results based on the latter. Section VI concludes the work by summarizing the key findings, evaluating the implications of the results, and discussing the broader significance of this type of benchmark.

II. DATA SETS

In the following, we motivate and introduce the data sets used within this study. These encompass two simple and well-studied data sets as well as an industrial image data set of practical relevance. The associated task for all data sets is a binary classification.

A. Data set 1 — linear split

The first data set is an artificial one and the only one not based on images. It is chosen with the premise of simplicity in mind and such that the ideal function, which classifies the data set perfectly, is known in advance. To this end, we choose to consider a d -dimensional hypercube, defined by the set $[0, 1]^d \subseteq \mathbb{R}^d$, and linearly split it by the plane orthogonal to the normal vector $\mathbf{n} = (1, 1, \dots, 1)^\top / \sqrt{d} \in \mathbb{R}^d$ which passes through the hypercube’s center $(1, 1, \dots, 1)^\top / 2 \in \mathbb{R}^d$. In order to generate training and validation data sets, we first place N data points randomly within the hypercube such that exactly $N/2$ points are located within each of the two sectors

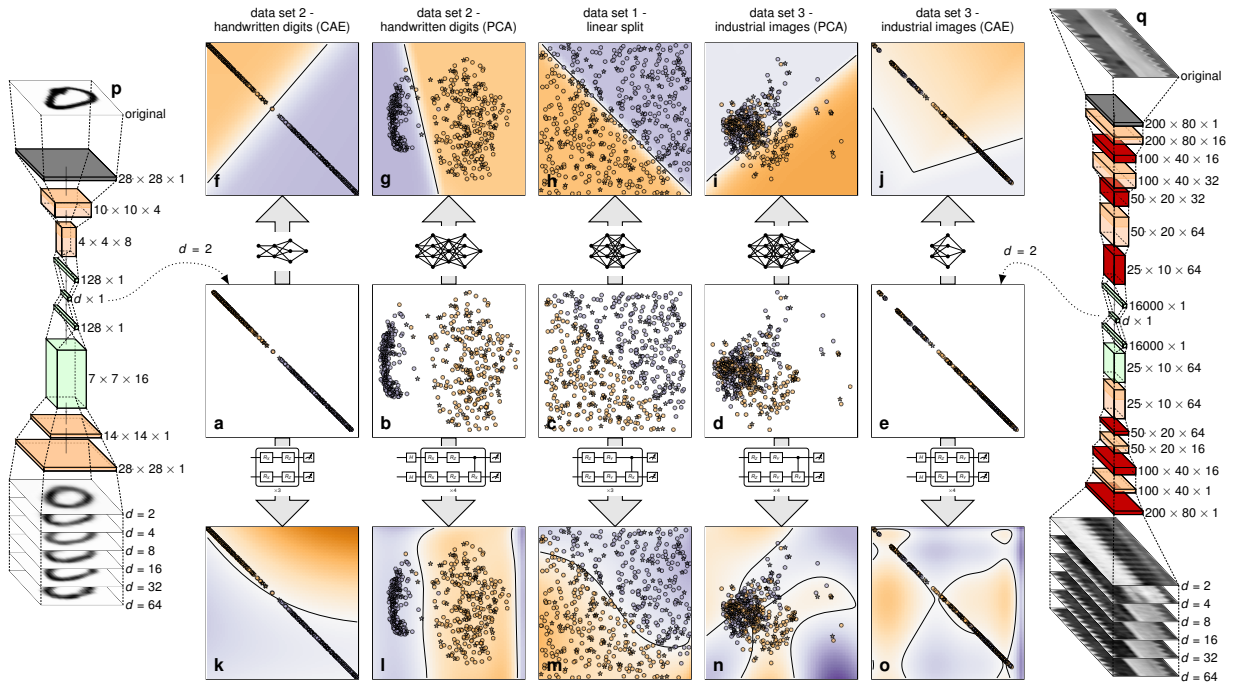


FIG. 1. Overview of data sets with $N = 500$ and dimension $d = 2$ in panels (a)-(e), and the corresponding learned functions by classical and quantum neural networks in panels (f)-(j) and panels (k)-(o), respectively. The small neural networks in between panels (a)-(e) and (f)-(j) show the best performing architectures (from among the set of randomly generated neural networks). The small quantum neural networks in between panels (a)-(e) and (k)-(o) show the respective best performing quantum architectures (from among the set of randomly generated quantum neural networks). Data points represented by circles (stars) in panels (a)-(o) correspond to the training (validation) data set. In addition, panels (p) and (q) show the architecture for the convolutional autoencoder (CAE) used to reduce the data dimensionality for the images of the second and third data set, respectively, as well as a representative illustration of the original and reconstructed images for various latent dimensions d .

separated by the hyperplane. These two sectors define the two labels that classify each data point. Afterwards, we split the N data points into training (validation) data sets consisting of $N_{\text{train}} = 0.8N$ ($N_{\text{val}} = 0.2N$) of the total data points. We perform this splitting so that the number of data points with each label within each subset is identical. In order to study the effect of the hypercube's dimension d and the data set size N , we generate versions of the hypercube data set with $d \in \{2, 4, 8, 16, 32, 64\}$ and $N \in \{200, 500, 1000, 2000\}$. An example with $d = 2$ and $N = 500$ is shown in Fig. 1 (c).

This hypercube data set has recently also been studied in a related work exploring the performance of quantum-machine-learning methods [16]. In this work, the hypercube data turned out to be rather difficult to classify by means of quantum-machine-learning methods, despite being a trivial problem for classical machine learning. Hence, we use it in our study as an ideal means to validate and benchmark our methodologies, introduced in Sec. III, and to check whether it can reproduce those results qualitatively.

B. Data set 2 — handwritten digits

As a second data set, we take the well-studied handwritten digits of the MNIST database [20] as another means to test our methodologies. However, in order to keep the classification problem binary, we restrict our study to images of 0's and 1's. Similar to the hypercube's data sets described in Sec. II A, we generate different versions of the MNIST data set with $N \in \{200, 500, 1000, 2000\}$ total images taken randomly from the 60000 available images. We again ensure that each generated data set has an equal number of 0's and 1's and that this ratio is maintained once the total data set is split into training and validation sets with $N_{\text{train}} = 0.8N$ and $N_{\text{val}} = 0.2N$ data points, respectively.

However, while the hypercube's data sets are artificial and their data dimension d is freely choosable, each of the MNIST images are 28×28 by default and hence consist of 784 unique features. While a data dimensionality of 784 is trivial to handle for classical neural networks, it is already challenging for fully-quantum machine-learning approaches in the present day. This is unfortunately true for its execution on actual quantum hardware as much as for any quantum models' simulation on classical computers. Thus, to make the MNIST images approachable

for quantum neural networks, which are used in one of our two methodologies employed to classify the data, we create dimensionality-reduced versions of the data. To this end, we consider again two different methods for dimensionality reduction as follows.

As a first method, we employ a principal component analysis (PCA). We fit it on all available images of 0's and 1's in the MNIST database and only afterwards apply it to the actual data sets used for training and validation with a total number of $N \in \{200, 500, 1000, 2000\}$ images. Due to this, we seek to prevent potential differences in the classification accuracy which might emerge, e.g. due to differences in data set sizes, having their origin in the PCA. We choose different levels of data reduction and fit PCAs using $d \in \{2, 4, 8, 16, 32, 64\}$ components in order to explore its impact on classification accuracies and to have identical dimensions to those generated for the hypercube data. At last, note that while the original MNIST images are rescaled and reshaped to vectors in $[0, 1]^{784}$ prior to applying the PCA, this normalization is broken by the PCA and we manually renormalize the PCA-reduced data vectors to $[0, 1]^d$ afterwards. This ensures that the final classical or quantum neural networks carrying out the actual classification only receive feature values from within $[0, 1]$. An example of the MNIST data that has been dimensionality-reduced via PCA with $d = 2$ and $N = 500$ is shown in Fig. 1 (b).

As a second method for dimensionality reduction, we employ a convolutional autoencoder (CAE). To this end, we design a classical convolutional encoder architecture which reduces the 28×28 input images to a latent space of dimension d and, after that, we use a decoder architecture to reconstruct the original image as best as possible. After having tested various architectures, we find the architecture illustrated in Fig. 1 (p) to work best for the MNIST images. This has been judged on the visual similarity of the original and reconstructed images, cf. the representative original and reconstructed images shown in the top and bottom of Fig. 1 (p), respectively. Furthermore, note that similarly to the PCA, the training of the CAE is first carried out using all available images of 0's and 1's from the MNIST database and the trained CAE is only applied afterwards to the actual data sets with a total number of $N \in \{200, 500, 1000, 2000\}$ data points. As latent dimension, we again choose and train CAEs for $d \in \{2, 4, 8, 16, 32, 64\}$. An example of the MNIST data that has been reduced via a CAE with $d = 2$ and $N = 500$ is shown in Fig. 1 (a). It is important to note that the employed CAEs apply an additional normalization by enforcing the sum of all features of the reduced d -dimensional data vector to be unity, thus effectively further reducing its dimension by one.

C. Data set 3 — industrial images

Our third and most important, as well as most challenging, data set consists of industrial images from laser



FIG. 2. Image of slats from a TRUMPF flatbed laser cutting machine. The slat in the front is in a good condition whereas the second slat has clear signs of wear and tear, such as tips that have melted away and slag splashes that adhere to the side. Image adapted from Ref. [34].

cutting machines designed for cutting sheet metal. Those machines feature supporting slats on which the sheet metal rests during processing. Physically, these slats are thin metal strips that span the width of the machine in a triangular pattern as illustrated in Fig. 2. In practice, their positions are regularly altered manually by adding or removing them from their respective sockets. However, for machine operation, it is advantageous to know their arrangement beforehand in order to take into account possible side-effects that their arrangement may cause [34], thus necessitating measurements prior to operation. Given the prominence of machine learning for automated image classification, visual methods have been identified previously as the most promising approach for accurately detecting the slats' positions [35]. Hence, we consider it a prototypical and industry-relevant image classification task.

In contrast to Fig. 2, the slat images we use in the following are already preprocessed and cut such as to focus on a single slat socket which may or may not contain a slat. The classification problem is thus binary with two difficulties arising due to varying camera angles from which the slat sockets are being photographed as well as the different condition of the slats, cf. Fig. 2. To ease data generation, TRUMPF has developed a model that generates synthetic slat socket images given the CAD model of the entire laser cutting machine and textures derived from real-world-resembling images using the Blender rendering engine. This way, manual labeling effort of real-world images is unnecessary and labeling errors are ruled out. Moreover, it allows to generate data sets with large image numbers. Identically to the other data sets, we consider different versions of this industry data set with $N \in \{200, 500, 1000, 2000\}$ total images, which are afterwards split into training and validation data sets with $N_{\text{train}} = 0.8N$ and $N_{\text{val}} = 0.2N$ data points, respectively. For these two sets, we ensure again the same class distribution as the original data set, as well as a similar number of images of slat sockets photographed with different camera angles and conditions. All images are gray-scale and normalized to 200×80 pixels independent of the photo

angle.

Similarly to the second data set, the images are too large to be directly processable by fully-quantum models, such as a quantum neural network. Hence, we create — again similarly to the second data set — dimensionality-reduced versions with either a PCA or CAE as the reduction method and fit either of the two methods to reduce the image data into d -dimensional data vectors. The reduction is separately fitted for $d \in \{2, 4, 8, 16, 32, 64\}$ and happens on all available slat images before being applied to the different versions of the third data set. For the CAE, after trying various architectures, we find the one illustrated in Fig. 1 (q) to work best for the slat images. An example of a 200×80 synthetic slat images is given at the top of Fig. 1 (q) and reconstructed versions from the various d 's at the bottom.

III. METHODOLOGY

As already indicated in Sec. II, the images of the second and third data sets are too large to be handled by fully-quantum machine-learning models. Hence, we employ two different methodologies in the following to classify them. The first of them being the usage of either classical and quantum neural networks to classify the dimensionality-reduced version of the previously introduced data sets. The other methodology being the usage of either classical or quantum-classical hybrid convolutional networks for classification which is applied to the full image data of the second and third data sets. In either of the two methodologies, the goal is a comparison of the performance between the fully-classical approach with the one involving quantum circuits as part of the total classification pipeline.

A. Methodology 1: Randomized neural networks

The first methodology, which acts on the dimensionality-reduced data sets, may be viewed as a two-stage protocol in order to classify the various data sets introduced in Sec. II. However, the first stage must be viewed as a mere necessity, as it is required to render the image data of the second and third data set approachable for quantum neural networks — an unpleasant but unfortunately currently inevitable step that enables the comparison of classical and quantum neural networks in the first place. It prepares the data such that the actual classification, which formally happens in the second stage, only receives data of moderate dimensionality which both the classical and quantum methods can handle. We are aware that this first data reduction step, if viewed independently from the second step, renders the classification task that is being solved in the second step much simpler, since a lot of the “heavy-lifting” is already solved in the first step. This is especially evident when viewing the reduced data for the handwritten digits from MNIST, independently

of whether a CAE or a PCA is used to reduce the original images, cf. Fig. 1 (a) and (b), respectively. In that case, even the dimensionality reduction to $d = 2$ features shows a very clear spatial separation of 0's and 1's, which already suggests a rather simple classification task for the second stage. In contrast, for the industrial images from TRUMPF, a reduction to $d = 2$ features seems too drastic in order to allow a proper reconstruction of the original image, cf. Fig. 1 (q) for a reduction via CAE although the results for a reduction via PCA are qualitatively similar. This is moreover evidenced by the reduced 2D data shown in Fig. 1 (d) and (e), where no clear spatial separation can be observed. In that case, a larger reduced dimensionality d is required, e.g. $d = 4$ or $d = 8$, to reproduce basic characteristics of the original image. Unfortunately, their corresponding data cannot be visualized trivially.

Having motivated and discussed the necessity of the dimensionality reduction of the first step, we now simply take its output data as input data for the second stage. From a mathematical point of view, the second stage thus gets a set $\mathcal{D} = \{(\mathbf{x}_i, y_i^{\text{true}})\}_{i=1, \dots, N_{\text{train}}}$ of vectors $\mathbf{x}_i \in \mathbb{R}^d$ and labels $y_i^{\text{true}} \in \{0, 1\}$, with N_{train} the number of training data points, that follows an unknown classification function $f: \mathbb{R}^d \rightarrow \{0, 1\}$ which needs to be learned — or approximated — by a machine-learning model given only \mathcal{D} . To do that, we consider both classical and quantum neural networks for classifying the data. In order to allow for an as fair as possible comparison between classical and quantum methods, we utilize a randomization scheme and generate classical and quantum neural networks with randomized hyperparameters. Their details are specified in Secs. III A 1 and III A 2, respectively. Through this, we ensure that we explore a larger — albeit not exhaustive — fraction of the individual hyperparameter spaces. As a consequence, this allows us to not only compare the best performing classical and quantum models generated this way, but also how average or badly performing models, which typically result from a poor choice of hyperparameters, compare between classical and quantum approaches.

In detail, we generate 50 random classical and quantum neural networks for each data set introduced in Sec. II. Since a model's performance, judged on the classification accuracy achieved on the validation data set, may depend strongly on the model's initial parameters which are used during training, we train each of the 50 classical and quantum models with 10 sets of random initial parameters. Each of the 10 sets is trained for up to 100 epochs, which suffices for convergence in almost all cases. As usual, we define one epoch as one complete pass through the training data set. This averaging heavily diminishes the effect of having exceptionally good or bad luck when choosing initial training parameters and shifts the focus to a model's average performance when — as in most cases — no a-priori knowledge about good initial trainable parameters is available. The performance of any of the 50 random classical or quantum models is thus given by the average of the 10 individual final classification accuracies achieved on the validation data set after training on the

training data set.

1. Classical neural networks

In order to generate random classical neural network architectures that allow processing of data vectors $\mathbf{x}_i \in \mathbb{R}^d$, there are various hyperparameters that can be randomly determined. Among the most prevalent ones are the number of dense, i.e., fully-connected, layers and the number of neurons per layer as well as the employed activation functions. We decide to randomize the first two by randomly choosing $n_{\text{layer},c} \in \{1, 2, 3, 4\}$ dense layers for each neural network, and independently choosing $n_{l,c} \in \{2, 3, 4\}$ neurons for each dense layer at random, with $l = 1, \dots, n_{\text{layer},c}$. Note that we actively decide to keep both numbers small in order to keep the models simple and the number of trainable parameters of the ensuing classical neural networks comparable to those of the quantum neural networks, whose randomized architectures are introduced in Sec. III A 2. While the number of trainable parameters is only one factor among many defining the (expressive) power of machine-learning models, with other factors being, for instance, their non-linearities, it is nevertheless a vital factor and its equivalence a prerequisite for comparability between different models — i.e., between classical and quantum architectures in our case. We thereby diminish the possibility that potentially better results for either classical or quantum neural networks are due to the fact that one has more trainable parameters available than the other. For the activation functions, we restrict our study to architectures where we use ReLU [36], defined as $\text{ReLU}(x) = \max(0, x)$, between every layer except for the final layer, which consists only of a single neuron for classification that is connected to its previous layer via the sigmoid activation function, defined as $\sigma(x) = (1 + e^{-x})^{-1}$.

While there are many other choices and hyperparameters to vary, such as the optimizer, the loss function or the learning rate, we decide to keep them fixed for all classical models in order to allow better comparability with quantum models¹. We choose the Adam optimizer [39], the mean squared error

$$\mathcal{L}_{\text{mse}} = \frac{1}{N_{\text{train}}} \sum_{i=1}^{N_{\text{train}}} (y_i^{\text{true}} - y_i^{\text{pred}})^2, \quad (1)$$

as the loss functions, with y_i^{true} and y_i^{pred} the true and predicted label of the i th data point, respectively, and a learning rate $R_c^{(1)} = 0.005$.

2. Quantum neural networks

In the following, we introduce how we generate random quantum neural network architectures, which, in practice, are given by parametrized quantum circuits (PQCs). To this end, note that their hyperparameters are — at least partially — very different from those of classical neural networks.

In view of quantum machine learning via PQCs, the solution to classification tasks, such as those described in Sec. II, can typically be divided into several steps, which we outline in the following before specifying our own adapted approach afterwards.

- (i) First, the initial state $|\Psi_{\text{init}}\rangle = |0\rangle^{\otimes n_q}$, with n_q the number of qubits, is prepared.
- (ii) Afterwards, the classical data from the vector $\mathbf{x}_i \in \mathbb{R}^d$ is encoded into the quantum state via a quantum feature map $S_{\text{enc}}(\mathbf{x}_i)$, i.e., $|\Psi_{\text{enc}}(\mathbf{x}_i)\rangle = S_{\text{enc}}(\mathbf{x}_i)|\Psi_{\text{init}}\rangle$.
- (iii) Then, a parametrized unitary $U(\boldsymbol{\theta})$, composed out of M_{param} parametrized quantum gates, with $\boldsymbol{\theta} \in \mathbb{R}^{M_{\text{param}}}$ the vector of gate parameters, is applied to yield $|\Psi_{\text{out}}(\mathbf{x}_i, \boldsymbol{\theta})\rangle = U(\boldsymbol{\theta})|\Psi_{\text{enc}}(\mathbf{x}_i)\rangle$.
- (iv) Finally, a measurement with a Hermitian operator O is performed to yield the expectation value $y_i^{\text{pred}}(\mathbf{x}_i, \boldsymbol{\theta}) = \langle \Psi_{\text{out}}(\mathbf{x}_i, \boldsymbol{\theta}) | O | \Psi_{\text{out}}(\mathbf{x}_i, \boldsymbol{\theta}) \rangle \in \mathbb{R}$.

The training aspect of this quantum-machine-learning ansatz is then to iteratively optimize the parameter vector $\boldsymbol{\theta}$ on a classical computer such that y_i^{pred} coincides with the true label y_i^{true} assigned by the unknown classification function $f : \mathbb{R}^d \rightarrow \{0, 1\}$ for all data points in $\mathcal{D} = \{(\mathbf{x}_i, y_i^{\text{true}})\}_{i=1, \dots, N_{\text{train}}}$. However, if trained successfully, the model ideally generalizes to data points $(\mathbf{x}', y') \notin \mathcal{D}$ beyond its training data set, but belonging to a source with the same distribution.

In order to adapt the above scheme to our approach of generating random quantum neural network models, there are various hyperparameters that can be varied. First, we allow for a random number n_q of qubits. In detail, to generate a random quantum neural network able to process d -dimensional input vectors, we choose $n_q \in \{2, 4, 8, \dots, d\}$ randomly, exploiting that d is always a power of two. Second, and intimately connected to the choice of n_q , is the choice of the quantum feature map $S_{\text{enc}}(\mathbf{x}_i)$, which, inspired by Refs. [24, 40–42], may become trainable as well in our case, i.e., $S_{\text{enc}}(\mathbf{x}_i, \boldsymbol{\phi})$ with $\boldsymbol{\phi} \in \mathbb{R}^{M_{\text{enc}}}$ a vector of M_{enc} trainable parameters. For simplicity, we first discuss the case $n_q = d$, since the case $n_q < d$ is more contrived. For $n_q = d$, the quantum feature map is chosen such that

$$S_{\text{enc}}(\mathbf{x}_i, \boldsymbol{\phi}) = \bigotimes_{n=1}^{n_q} R_{\alpha, n} (f_{\text{enc}}(x_{i,n}, \phi_n)) \quad (2)$$

¹ This is primarily because the employed software for the quantum neural networks [37] provides less options than that employed for the classical neural networks [38]

where $R_{\alpha,n}(\beta) = \exp\{-i\alpha\beta/2\}$ is a rotational single-qubit gate, applied to the n th qubit, parametrized by an angle β and specified by the Pauli operator $\alpha \in \{X, Y, Z\}$. The latter is chosen randomly but identical for all n_q qubits. This encoding scheme, i.e., to encode one feature $x_{i,n}$ per qubit, has been identified previously as a viable embedding scheme [43, 44]. The encoding function $\beta = f_{\text{enc}}(x_{i,n}, \phi_n)$ is also chosen randomly from a set of predefined functions $f(x, \phi)$ encompassing the functions

$$\{x, \arccos(x), x + \phi, x\phi, \arccos(x)\phi\}. \quad (3)$$

Note that some functions are accompanied by an additional trainable parameter ϕ while some just contain the feature value x . The inclusion of $\arccos(x)$ as a non-linearity is inspired by Ref. [5]. In total, this randomized quantum feature map $S_{\text{enc}}(\mathbf{x}_i, \boldsymbol{\phi})$ produces the encoded state $|\Psi_{\text{enc}}(\mathbf{x}_i, \boldsymbol{\phi})\rangle$ to which we then apply a parametrized unitary $U(\boldsymbol{\theta})$ consisting of randomly chosen gates as follows. First, we apply another randomized but identical single-qubit rotational gate $R_{\alpha,n}(\beta)$ to each qubit $n = 1, \dots, n_q$, where, this time, $\beta = \theta$ is plainly a trainable parameter from $\boldsymbol{\theta} \in \mathbb{R}^{M_{\text{param}}}$. This is followed by a randomized choice of having no entangling gates or any of the three controlled $cR_{\alpha}(\beta)$ gates, $\alpha \in \{X, Y, Z\}$, defined via

$$cR_{\alpha}(\beta) = |0\rangle\langle 0|^{\text{ctrl}} \otimes \mathbb{1}^{\text{trgt}} + |1\rangle\langle 1|^{\text{ctrl}} \otimes R_{\alpha}^{\text{trgt}}(\beta) \quad (4)$$

with superscripts ‘‘ctrl’’ and ‘‘trgt’’ denoting control and target qubit, respectively. If the randomization chooses to have entangling gates, this implies that several of them are being placed, with each of them having their own trainable parameter. We choose randomly between two possible structures. On the one hand, we may choose to have a

linear structure in the sense that there is an entangling gate between qubits 1 and 2, between 2 and 3 and so on until qubits $n_q - 1$ and n_q . On the other hand, we may choose an all-to-all connected structure, i.e., an entangling gate between any pair of qubits. Note that the difference only matters for $n_q > 2$. The single-qubit rotational gates together with the randomized trainable entangling gates make up the parametrized quantum circuit $U(\boldsymbol{\theta})$.

As another choice of randomization and inspired by Refs. [22, 23], which motivate the repetition of the data encoding and the parametrized circuit to enhance a model’s expressivity, we randomly choose to execute $n_{\text{layer,q}} \in \{1, 2, 3, 4\}$ layers of the quantum feature map and the parametrized unitary. Our randomized PQC (for $n_q = d$) thus reads

$$U_{\text{pqc}}(\mathbf{x}_i, \boldsymbol{\phi}, \boldsymbol{\theta}) = U_{\text{had}} \prod_{l=1}^{n_{\text{layer,q}}} [U(\boldsymbol{\theta}_l) S_{\text{enc}}(\mathbf{x}_i, \boldsymbol{\phi}_l)], \quad (5)$$

where $\boldsymbol{\phi}_l$ and $\boldsymbol{\theta}_l$ are trainable parameters that are independent for each layer l despite $S_{\text{enc}}(\mathbf{x}_i, \boldsymbol{\phi}_l)$ and $U(\boldsymbol{\theta}_l)$ having the same overall structure in each layer. As a final choice of randomizing the PQC, the additional unitary U_{had} randomly applies either a Hadamard gate or the identity to all qubits. This is a means to rotate the initial state $|\Psi_{\text{init}}\rangle = |0\rangle^{\otimes n_q}$ into a more accessible basis prior to executing the remainder of the PQC.

Having so far discussed the case $n_q = d$, we now discuss $n_q < d$. In those cases, the quantum feature map, as introduced in Eq. (2), cannot be directly used since there are fewer qubits than there are features that need encoding. However, we can choose the same structure as in the final PQC of Eq. (5) and adapt it to have multiple quantum feature maps that each encode a fraction of the total data vector $\mathbf{x}_i \in \mathbb{R}^d$. In detail, we adapt Eq. (5) to become

$$U_{\text{pqc}}(\mathbf{x}_i, \boldsymbol{\phi}, \boldsymbol{\theta}) = U_{\text{had}} \prod_{l=1}^{n_{\text{layer,q}}} \left[\prod_{r=1}^{n_{\text{rep}}} [U_r(\boldsymbol{\theta}_{l,r}) S_{\text{enc},r}(\mathbf{x}_{i,r}, \boldsymbol{\phi}_{l,r})] \right], \quad (6)$$

where $\mathbf{x}_{i,r} \in \mathbb{R}^{n_q}$ are fractions of $\mathbf{x}_i = (\mathbf{x}_{i,1}, \dots, \mathbf{x}_{i,n_{\text{rep}}}) \in \mathbb{R}^d$ with $n_{\text{rep}} = d/n_q$. Note that we allow the quantum feature maps $S_{\text{enc},r}(\mathbf{x}_{i,r}, \boldsymbol{\phi}_{l,r})$ and the parametrized unitary $U_r(\boldsymbol{\theta}_{l,r})$ to be chosen differently in every repetition $r = 1, \dots, n_{\text{rep}}$, following the same randomization procedure as introduced before. However, their randomly chosen architectures are again identical for each layer $l = 1, \dots, n_{\text{layer,q}}$. In contrast, their trainable parameters $\boldsymbol{\phi}_{l,r}$ and $\boldsymbol{\theta}_{l,r}$ are different in each repetition and layer.

To finally map the output state

$$|\Psi_{\text{out}}(\mathbf{x}_i, \boldsymbol{\phi}, \boldsymbol{\theta})\rangle = U_{\text{pqc}}(\mathbf{x}_i, \boldsymbol{\phi}, \boldsymbol{\theta}) |\Psi_{\text{init}}\rangle \quad (7)$$

to a scalar, we need to specify the measurement operator O . Within our randomization approach, we make it train-

able as well and allow it to be one of the two following operators at random,

$$O_{\text{pauli}}(\boldsymbol{\omega}) = \omega_1 \mathbb{1} + \sum_{n=1}^{n_q} (\omega_{n,x} X_n + \omega_{n,y} Y_n + \omega_{n,z} Z_n) \quad (8a)$$

or

$$O_{\text{ising}}(\boldsymbol{\omega}) = \omega_1 \mathbb{1} + \sum_{n=1}^{n_q} (\omega_{n,x} X_n + \omega_{n,z} Z_n) + \sum_{\substack{n,m=1 \\ n < m}}^{n_q} \omega_{nm} Z_n Z_m, \quad (8b)$$

where $\boldsymbol{\omega} \in \mathbb{R}^{M_{\text{op}}}$ captures the M_{op} trainable parameters of $O_{\text{pauli}}(\boldsymbol{\omega})$ or $O_{\text{ising}}(\boldsymbol{\omega})$. Ultimately, this yields the

expectation value

$$y_i^{\text{pred}}(\mathbf{x}_i, \boldsymbol{\phi}, \boldsymbol{\theta}, \boldsymbol{\omega}) = \langle \Psi_{\text{out}}(\mathbf{x}_i, \boldsymbol{\phi}, \boldsymbol{\theta}) | \mathcal{O}(\boldsymbol{\omega}) | \Psi_{\text{out}}(\mathbf{x}_i, \boldsymbol{\phi}, \boldsymbol{\theta}) \rangle. \quad (9)$$

The training process for the PQC is then to optimize the circuit parameters $\boldsymbol{\phi}$ and $\boldsymbol{\theta}$ as well as the operator parameter $\boldsymbol{\omega}$ in order to match $y_i^{\text{pred}}(\mathbf{x}_i, \boldsymbol{\phi}, \boldsymbol{\theta}, \boldsymbol{\omega})$ and y_i^{true} as best as possible for all N_{train} data points in \mathcal{D} . Although this process is intended to be carried out in a quantum-classical hybrid approach, as described earlier, note that we carry out all our simulations on classical computers, involving extensive simulations of quantum circuits on a high-performance computing infrastructure. Furthermore, note that the randomization procedure described so far has a small but non-vanishing probability of yielding non-trainable models, for instance, by exclusively adding diagonal gates like R_z and cR_z to the PQC unitary U_{pqc} , which thus becomes diagonal as well and produces $|\Psi_{\text{out}}(\mathbf{x}_i, \boldsymbol{\phi}, \boldsymbol{\theta})\rangle = e^{i\varphi} |\Psi_{\text{init}}\rangle$ with φ some phase. The latter is the only variable that will change while training such a PQC, which invalidates such PQCs for practical machine-learning tasks. We do not neglect these models per se but exclude them in any analysis where they would otherwise distort the statistics.

We employ again the Adam optimizer, use the squared error

$$\mathcal{L}_{\text{se}} = \sum_{i=1}^{N_{\text{train}}} (y_i^{\text{true}} - y_i^{\text{pred}})^2, \quad (10)$$

as the loss function and the learning rate $R_q^{(1)} = 0.05$ ².

B. Methodology 2: Convolutional neural networks

As already mentioned when introducing the first methodology in the previous Sec. III A, the employed dimensionality reduction is a mere necessity — but one that heavily alters the classification problem being solved in its second stage. For our second methodology, we therefore avoid such dimensionality reduction methods and directly classify the full image data. However, while this is feasible for fully-classical models, it is still not feasible for fully-quantum models. This is why we now resort to a comparison between fully-classical and quantum-classical hybrid models, although in a way that dimensionality reduction is not needed. The hybrid models considered for this methodology consist of hybridizations of convolutional neural networks with quantum neural networks used as analogs of their convolution filters, which in classical convolutional layers are simple matrices. This hybrid

model structure was first explored in Ref. [21]. One should not confuse these models with the ones referred to as quantum convolutional neural networks (QCNNs) [31], which are essentially fully-quantum neural networks that progressively trace out qubits in the middle of the circuit using, for instance, mid-circuit measurements. The latter are responsible for preventing barren plateaus in these models [32] and also add non-linearity to the quantum operations. However, they also make QCNNs classically simulable [18]. Since the hybrid models used are much more computationally expensive to train due to many applications of each quantum circuit, we opt to preselect a smaller set of combinations of hyperparameters instead of relying on the randomization approach used before. However, we still train each model with 10 different sets of random initial parameters for 100 epochs to ensure that the results are not biased by the choice of initial parameters.

We compare these hybrid models to fully-classical convolutional neural networks, which are a standard tool for image classification tasks. To ensure a fair comparison, we also preselected a set of combinations of hyperparameters for these models. We opted to not include the linear-split data set, cf. Sec. II A, in our convolutional neural network experiments. This decision stems from a fundamental mismatch between the inductive biases of convolutional neural networks and the mathematical structure of the hypercube classification problem. Convolutional operations are designed to exploit spatial locality, translation invariance and hierarchical feature composition. These properties are naturally present in image data, as we further describe in Sec. III C. However, the linear split of a hypercube represents a purely geometric problem where features lack meaningful spatial relations. In fact, each dimension of the hypercube corresponds to an independent coordinate rather than a spatially correlated pixel, making convolution operations conceptually inappropriate for this task. Thus, including this data set could potentially lead to misleading conclusions about the relative performance of classical and quantum approaches.

The details of the used classical and hybrid convolutional neural networks are specified in Sec. III B 1 and Sec. III B 2, respectively.

1. Classical convolutional neural networks

Classical convolutional neural networks, in the following referred to as CNNs, which we use in this second methodology with the full, non-reduced image data sets, allow for the processing of data matrices $\mathbf{X}_i \in \mathbb{R}^{n_h \times n_w}$, where n_h and n_w are the number of pixels in the height and width of the corresponding image, respectively.

The key distinction between CNNs and classical neural networks is the exchange of simple matrix multiplications in dense layers — which are linear operations — for discrete convolutions in convolutional layers — which are

² Note that we use a larger learning rate for the quantum neural networks, compared to their classical counterparts, in order to achieve a similar convergence behavior given the different loss functions

non-linear. A discrete convolution operation is defined as

$$(\mathbf{X} * \mathbf{K})_{i,j} = \sum_{m=0}^{k_h-1} \sum_{n=0}^{k_w-1} \mathbf{X}_{i+m,j+n} \mathbf{K}_{m,n}, \quad (11)$$

where $*$ denotes the convolution operation, \mathbf{X} is the input matrix, \mathbf{K} is the filter matrix, the indices i and j denote the entry (i, j) of the output matrix, and k_h and k_w are the dimensions of the filter matrix. The entries of the filter matrix are the trainable parameters of the convolutional layer, which can have multiple filters. The output of the convolution operation represented in Eq. (11) is a matrix with dimensions $n_h \times n_w$, the same as the input matrix. However, in CNNs, the filter matrix can be applied to only some $k_h \times k_w$ submatrices of the input matrix, with a stride s determining the step size between each application of the filter along both image axes. Then, the output of the convolution operation is a matrix with dimensions $d_{f,c}^h \times d_{f,c}^w$, where $d_{f,c}^h = (\hat{n}_h - k_h)/s + 1$ and $d_{f,c}^w = (\hat{n}_w - k_w)/s + 1$. Here, \hat{n}_h and \hat{n}_w are the dimensions of the input matrix after padding it, for instance, with zeros to ensure that the filter can be applied to the edges of the original image.

Some of the typical hyperparameters which can be varied in CNNs are the number of convolutional layers, the number of filters per convolutional layer, the size of these filters, the stride of each convolution, and the use of additive biases in each convolution operation. The latter are trainable parameters which are added to the output of a convolution operation.

To mimic the chosen structure for the hybrid CNNs, described in the following Sec. III B 2, we opted to use CNNs consisting of one usual convolutional layer followed by a varying number n_{dconv} of depth-wise convolutional layers. These depth-wise convolutional layers differ from usual convolutional layers for input images with multiple channels, i.e., with a third dimension $d_3 > 1$. The depth-wise convolutional layers convolve a different filter matrix with each output channel of the previous layer, instead of applying each filter to the entire input image, which effectively makes the filters 3-dimensional, with the third dimension equal to d_3 . Thus, applying usual convolutions after the first convolutional layer would require 3-dimensional filters if the previous layer used more than one filter, which would increase the number of trainable parameters significantly. This choice was again made to mimic the structure of the hybrid CNNs. The outputs of the convolutional layers are flattened into a vector and processed by a dense layer with two neurons and a softmax activation function, defined as $\text{softmax}(\mathbf{x})_i = e^{x_i} / \sum_{j=1}^n e^{x_j}$, where i is the index of the class for which we calculate the softmax value and $n = 2$ is the number of classes in our problem. The softmax function is used to transform the outputs into a probability distribution over the predicted output classes.

To mimic the hyperparameter sets chosen for the hybrid CNNs, we opted for using filters with sizes 2×2 or 3×3 for all convolutional layers. For the first convolutional layer, we chose strides equal to the size of the filters, such that each filter is applied once to each image pixel.

Depending on the choice of filter size, we use either four or nine filters in the first convolutional layer, respectively. For the depth-wise convolutional layers, we convolve each output channel of the previous layer with a single filter and a stride of step size $s = 1$, to guarantee that the dimension of the input to the dense layer remains the same whether we use depth-wise convolutional layers or not. This way, we can focus our analysis on the number of trainable parameters in the convolutional layers, since the dense layers will have the same number of parameters, regardless of the number of convolutional layers we use. In order to have between one and three convolutional layers, we tested the number of depth-wise convolutional layers $n_{\text{dconv}} \in \{0, 1, 2\}$. We also decided to test the introduction of additive biases in all convolutional layers at once.

Since we fix the model structures in the second methodology, it is simple to calculate the number of trainable parameters in these networks formally. Therefore, the considered CNNs have a total number of trainable parameters M_{cnn} given by

$$M_{\text{cnn}} = M_{\text{conv}} + M_{\text{dense}}, \quad (12a)$$

$$M_{\text{conv}} = [(k_h k_w)^2 + \delta_b k_h k_w] l, \quad (12b)$$

$$M_{\text{dense}} = \frac{2\hat{n}_h \hat{n}_w k_h k_w}{s^2} + 2, \quad (12c)$$

where M_{conv} is the number of parameters in the convolutional layers, M_{dense} is the number of parameters in the final dense layer, and $\delta_b \in \{0, 1\}$ indicates if the convolutions have additive biases or not.

We again use the Adam optimizer with a learning rate $R_c^{(2)} = 0.01$ and the cross entropy

$$\mathcal{L}_{\text{ce}} = - \sum_{i=1}^{N_{\text{train}}} \sum_{j=1}^{n_{\text{class}}} y_j^{\text{true}} \log(y_{i,j}^{\text{pred}}), \quad (13)$$

as the loss function, where $n_{\text{class}} = 2$ is the number of classes in our problem, y_j^{true} represents the class j , in our case $y_1^{\text{true}} = 0$ and $y_2^{\text{true}} = 1$, and $y_{i,j}^{\text{pred}}$ is the predicted probability of the i th input image belonging to class j . This loss function measures the difference between the predicted probability distribution and the true distribution of the labels in the training data set.

2. Quantum-classical hybrid convolutional neural networks

As mentioned before, the quantum-classical hybrid convolutional neural networks, in the following referred to as QCCNNs — for “quantum-classical CNNs” — use PQCs instead of classical convolutional layers to process the input data. While the structure of these QCCNNs is inspired by Ref. [21], the quantum circuits we use are fully trainable instead of fixed.

The structure of the studied QCCNNs is the same as that of the CNNs, cf. Sec. III B 1, with the exception that all convolutional layers are replaced by a single quantum convolution. The latter is defined as a direct analogue

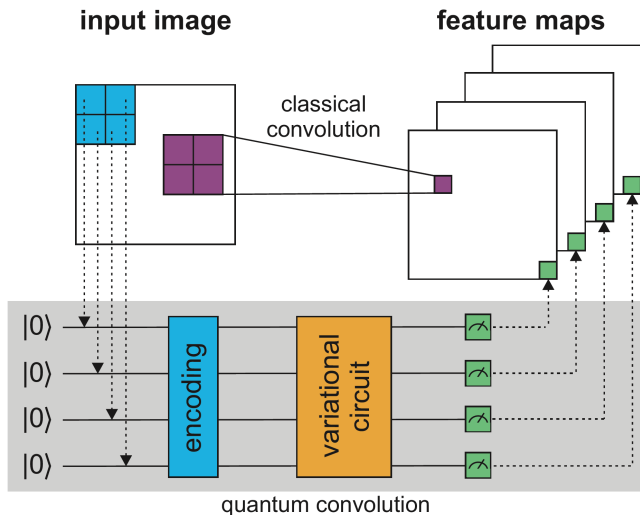


FIG. 3. Example scheme of a quantum convolution operation using a filter with dimensions 2×2 and a PQC with four qubits. In our QCCNN models, the input matrices are the non-reduced images, either from the handwritten-digit or the industrial-image data sets, cf. Secs. IIB and IIC, and the output feature maps are flattened into a vector and fed to a classical dense layer. A minimal representation of an analogue classical convolution with the same filter size is also shown. Image adapted from Ref. [45].

of the classical discrete convolution, whereby the input matrix is “quantum convolved” with a PQC by encoding the pixels of each $k_h \times k_w$ submatrix of the input matrix — defined by the “quantum-filter” size and stride s of the (quantum) convolution as in the classical case — into the PQC and measuring the expectation value of an observable on the chosen qubits of the output state. The output of the quantum convolution is a 3-tensor of expectation values of observables, whose first two dimensions are dependent on the size of the input matrix and the third dimension is dependent on the number of measured qubits in the PQC. This output has dimensions $d_{f,q}^h \times d_{f,q}^w \times n_{q,\text{meas}}$, where $d_{f,q}^h = d_{f,c}^h$, $d_{f,q}^w = d_{f,c}^w$

(cf. Sec. III B 1), and $n_{q,\text{meas}}$ is the number of measured qubits. Figure 3 illustrates an example of the quantum convolution operation described above, with four qubits, as well as how it compares to a classical convolution. Note that, in this example, we would need four classical convolutional filters to obtain an output of the same dimensions as the one with the quantum convolution. The output of the quantum convolution is then flattened into a vector, which is then classified by classical means, i.e., by a dense layer of two neurons and a softmax activation function, similar to the fully-classical case.

Considering a stride of $s = 1$ for simplicity, the formula for the $n_{q,\text{meas}}$ -vector at position (i, j) of the output 3-tensor of a quantum convolution with a quantum filter with dimensions $k_h \times k_w$, as a function of its PQC, is

$$(\mathbf{X} * U_{\text{PQC},\phi,\theta})_{i,j} = U_{\text{PQC}}(\mathbf{X}_{i,i+k_h-1,j,j+k_w-1}, \phi, \theta), \quad (14)$$

where ϕ represents a tensor of all trainable parameters used in the quantum feature map of the PQC, θ represents a tensor of all gate parameters used in the following trainable unitaries, and $\mathbf{X}_{i,i+k_h-1,j,j+k_w-1}$ is the submatrix of \mathbf{X} which can be defined by its upper left corner at position (i, j) and its lower right corner at position $(i + k_h - 1, j + k_w - 1)$, thus having the dimensions of the quantum filter.

For the QCCNNs, we also use quantum-filter sizes of 2×2 and 3×3 with strides equal to the size of the filters, i.e., $s = 2$ and $s = 3$, respectively. To simplify the PQC structures, we encode only one feature per qubit, such that the width n_q of the PQC is defined by the quantum filter size, $n_q = k_h k_w$, i.e., $n_q = 4$ for 2×2 filters and $n_q = 9$ for 3×3 filters.

Since we fix a smaller set of combinations of hyperparameters, we need to ensure we benchmark models which are still expressive enough. To this end, with the insight that the choice of the quantum feature map $S_{\text{enc}}(\mathbf{x}_i, \phi)$ directly lower-bounds the smallest training error achievable [46], we opt for a very expressive trainable feature map of the form

$$S_{\text{enc}}(\mathbf{x}_i, \phi) = \bigotimes_{n=1}^{n_q} R_n(f_{\text{enc}}(x_{i,n}, \phi_{1,n}), f_{\text{enc}}(x_{i,n}, \phi_{2,n}), f_{\text{enc}}(x_{i,n}, \phi_{3,n})), \quad (15)$$

where $R_n(\alpha, \beta, \omega) = R_{Z,n}(\omega)R_{Y,n}(\beta)R_{Z,n}(\alpha)$ (cf. Sec. III A 2 for the definition of the individual gates) is a general single-qubit rotation gate applied to the n th qubit and parametrized by the three angles α, β, ω . The encoding function f_{enc} is fixed by the non-linear form $f_{\text{enc}}(x, \phi) = \arccos(x)\phi$ for all three angles. While we encode each pixel $x_{i,n}$ in all angles of this general rotation, each angle has its own trainable parameter,

$\phi_{j,n}, j \in \{1, 2, 3\}$. This quantum feature map receives as input a submatrix flattened into a vector $\mathbf{x}_i \in \mathbb{R}^{n_q}$, and a matrix of trainable parameters $\phi \in \mathbb{R}^{3 \times n_q}$.

We decided to test QCCNNs with one of two entangling structures, namely circular entanglement, which is similar to the linear structure described in Sec. III A 2 but with an additional entangling gate between qubits n_q and 1; and all-to-all entanglement, described in the same Section.

We fix the entangling gates used in all QCCNNs with the form $cR_X(\theta)$, with θ being a trainable parameter specific to each gate. Additionally, we also test QCCNNs without entangling gates to benchmark the usefulness of entanglement in these hybrid models for the classical data sets tested.

As with the approach based on randomized quantum neural networks defined in Sec. III A 2, we define a quantum layer as the quantum feature map followed by trainable entangling gates. In practice, we test PQCs with $n_{\text{layer,q}} \in \{1, 2, 3\}$ quantum layers. This is a direct analogy of the convolutional-layer structure used in the classical CNNs. However, in contrast to the measurement operators employed by the randomized quantum neural networks, cf. Eqs. (8a) and (8b), we fix the measurement observable for each qubit as the Pauli Z operator.

The PQCs we use in the QCCNNs take the form

$$U_{\text{pqc}}(\mathbf{x}_i, \phi, \theta) = \prod_{l=1}^{n_{\text{layer,q}}} \left[U(\theta_l) S_{\text{enc}}(\mathbf{x}_i, \phi_l) \right], \quad (16)$$

where $U(\theta_l)$ represents the unitary describing the application of the parametrized entangling gates after the quantum feature map for each layer l of the PQC.

The QCCNNs described so far have a number of trainable parameters given by

$$M_{\text{qccnn}} = (M_{\text{enc}} + M_{\text{ent}}) n_{\text{layer,q}} + M_{\text{dense}}, \quad (17a)$$

$$M_{\text{enc}} = 3k_h k_w, \quad (17b)$$

$$M_{\text{dense}} = \frac{2\hat{n}_h \hat{n}_w k_h k_w}{s^2} + 2, \quad (17c)$$

where M_{enc} is the number of parameters in one application of the quantum feature map, M_{ent} is the number of parameters in the entangling gates of each layer and M_{dense} is the number of parameters in the final dense layer. For QCCNNs with circular entangling gates, $M_{\text{ent}} = k_h k_w$, while for those with all-to-all entangling gates, $M_{\text{ent}} = [k_h k_w (k_h k_w - 1)]/2$. Obviously, for QCCNNs without entangling gates, $M_{\text{ent}} = 0$.

We highlight that the CNNs and QCCNNs we consider have a very similar number of parameters, only differing slightly in the number of parameters in their convolutions. For the scenarios we consider in the following, specifically for the handwritten-digit data set with 2×2 (3×3) convolution filters, the dense layer has $M_{\text{dense}} = 1570$ (1802) parameters, with the difference originating from image padding. However, due to the much larger dimensions of the industrial images, this data set brings the number of parameters of the dense layer to $M_{\text{dense}} \approx 32000$. In fairness, most of the parameters of both CNNs and QCCNNs belong to their final dense layer. Thus, we find it reasonable to benchmark all models against a single classical dense layer with two neurons and softmax activation function as a baseline. Moreover, we note the number of parameters in the models of the second methodology is much larger than in the randomized models of the first methodology. The presumable increase in the models

expressivity, compared to that of the first methodology, is necessary for them to be able to extract useful information from the original and non-reduced 784 or 16000 image features. This is in contrast to the first methodology where models need to extract information from at most 64 features.

Given the similar structures between classical and hybrid CNNs, we decide to use the same optimizer, learning rate $R_q^{(2)} = R_c^{(2)}$, and loss function as with classical CNNs, cf. Sec. III B 1.

As mentioned before, these hybrid models are computationally expensive due to the many applications of the PQC in the quantum convolution. For instance, for a 2×2 quantum filter with stride $s = 2$, each image of the handwritten-digit data set requires 196 applications of the 4-qubit PQC per iteration. For the industrial data set in the same scenario, this figure increases to 4000. Hence, since all the models were simulated on classical hardware, this study was only possible through the use of high-performance computing infrastructure paired with just-in-time (JIT) compilation of our code. Even then, the longest simulation of a QCCNN still took ~ 5 days for each set of random initial parameters. This was the case for the QCCNN with a 3×3 quantum filter, stride of $s = 3$, and a 9-qubit PQC with all-to-all entanglement and $n_{\text{layer,q}} = 3$ layers, applied on the industrial-image data set with $N = 500$ data points.

C. Limits of the methodologies

In the following, we want to briefly summarize our methodologies and point out possible limitations in order to provide a clear picture to the reader.

For the first methodology, cf. Sec. III A, we use randomized classical and quantum neural networks to classify dimensionality-reduced data sets, cf. Sec. II. Since the dimensionality reduction is done via fully-classical methods, either by PCA or CAE, comparing the performances of classical and quantum neural networks in classifying the data becomes a comparison between fully-classical and quantum-classical hybrid methods. Moreover, to ensure a fairer comparison, we restrict the size of the classical neural networks such that they have a similar number of trainable parameters compared to their quantum counterparts. For the quantum neural networks, restricting them to modest sizes is necessary, on the one hand, to keep them in the feasible computational regime of current and near-term quantum hardware, and, on the other hand, to keep them classically simulable. At last, we note that we generate neural networks randomly instead of performing a structured hyperparameter search. This allows us to explore a larger fraction of the hyperparameter space.

In the second methodology, cf. Sec. III B, we avoid dimensionality reductions via PCA or CAE for the image data, but apply classical or quantum convolutional layers on the full image data. Afterwards, its output is transferred to a classical dense layer responsible for the final

classification. Hence, this methodology is a comparison between fully-classical and quantum-classical hybrid methods as well. Moreover, this methodology is numerically expensive to simulate, which is why we avoid randomization of the convolutional layer structures, but restrict ourselves to some preselected ones. In contrast to the first method, we do not use optimizable measurements or randomized types of entangling gates. In this case, only the structure of the entangling gates is randomized.

The literature suggests that optimal performance often depends on the alignment between a model’s inherent assumptions — its inductive biases — and the underlying structure of the data [47]. Each methodology has its associated inductive biases and is suited for different types of data or learning objectives. In our first methodology, the randomized hyperparameter approach diversifies these biases. Nevertheless, the models used are still relatively simple. Both the classical and quantum neural networks incorporate minimal inductive biases beyond basic function approximation, hopefully allowing them to learn relatively unconstrained representations of the dimensionality-reduced data. At the same time, this means that the models may not be able to fully exploit the underlying structure of each data set, especially the more complex industrial image data set.

On the other hand, the CNNs in our second methodology have strong inductive biases toward spatial locality, translation invariance, and hierarchical feature composition, as described in Sec. III B. These biases are fundamentally designed with images in mind. They aim to exploit the assumption that neighboring pixels often contain related information and that similar useful patterns can appear at different spatial locations. QCCNNs inherit these spatial biases from their convolutional-like procedure, while introducing different quantum-specific inductive biases through their PQCs. Hence why, in this methodology, we focus on image data sets.

Moreover, the dimensionality reduction methods used in the first methodology, PCA and CAE, favor different inductive biases themselves. Since this can further skew the benchmark results for general binary image classification tasks, we opted to use both methods in our analysis.

Nevertheless, we must note that we did not consider the specific inductive biases of each generated model, especially in the first methodology. Instead, we treat quantum architectures as black boxes which we explore through randomization. Thus, our methodology distinguishes itself from other works that specifically design PQCs to exploit known structures in the data, such as linearly conserved quantities or data-ordering effects [47, 48].

For both methodologies, we assess model performance with a focus on their classification accuracies after 100 epochs of training, even though an argument can be made for comparing other performance metrics, such as the convergence speed for similar accuracies or the robustness to different hyperparameter choices. The learning rates are also not changed or optimized. While we tested various learning rates initially, we did not observe a noticeable

impact on the model’s final classification accuracy after 100 training epochs. Hence, we fixed the rates to those mentioned before as they reliably ensure convergence of the classification accuracy in almost all cases. At last, we note that we did not include noise in the quantum models even though this will most likely lead to lower performance of the quantum models.

IV. RESULTS FROM RANDOM NEURAL NETWORKS

In this section, we exclusively present and discuss the results obtained by employing the methodology based on randomized classical and quantum neural networks, introduced in Sec. III A, and applied to all data sets from Sec. II.

A. Comparison of classical and quantum neural network performances

1. Detailed discussion of data set 3 — industrial images — under PCA reduction

Classical models — We start discussing our results by immediately comparing the performances of the 50 random classical and quantum neural networks in their ability to correctly classify the various versions of the industrial image data set, cf. Sec. II C, since we believe them to be the most important ones. We start with the various versions distinguished by their number of data points $N \in \{200, 500, 1000, 2000\}$ and their reduced dimensionality $d \in \{2, 4, 8, 16, 32, 64\}$ employing PCA as the reduction method. The results for the first and second data sets, as well as the third data set when employing a CAE as the dimensionality reduction method, are discussed afterwards.

Figure 4 (a) shows the classification results for each of the 50 randomly generated classical neural networks in orange colors. For the simplest classification task with $d = 2$, our randomization methodology generates no models which perform excellently, i.e., yielding averaged classification accuracies close to 100%. In fact, even the best models do not surpass classification accuracies of around $\sim 75\%$ while the worst ones are just slightly above 50%. There is, however, a notable difference depending on the size of the training data set. Unless for the smallest one with $N = 200$, the larger data sets yield at best classification accuracies at around 60%. Given the rather drastic data reduction down to $d = 2$ features, the poor overall classification accuracies are no surprise and the slightly better performance in case of $N = 200$ may be attributed to an artificially less complex task determined by the small validation data set. Figure 1 (i) exemplarily shows the data points as well as the learned function that classifies

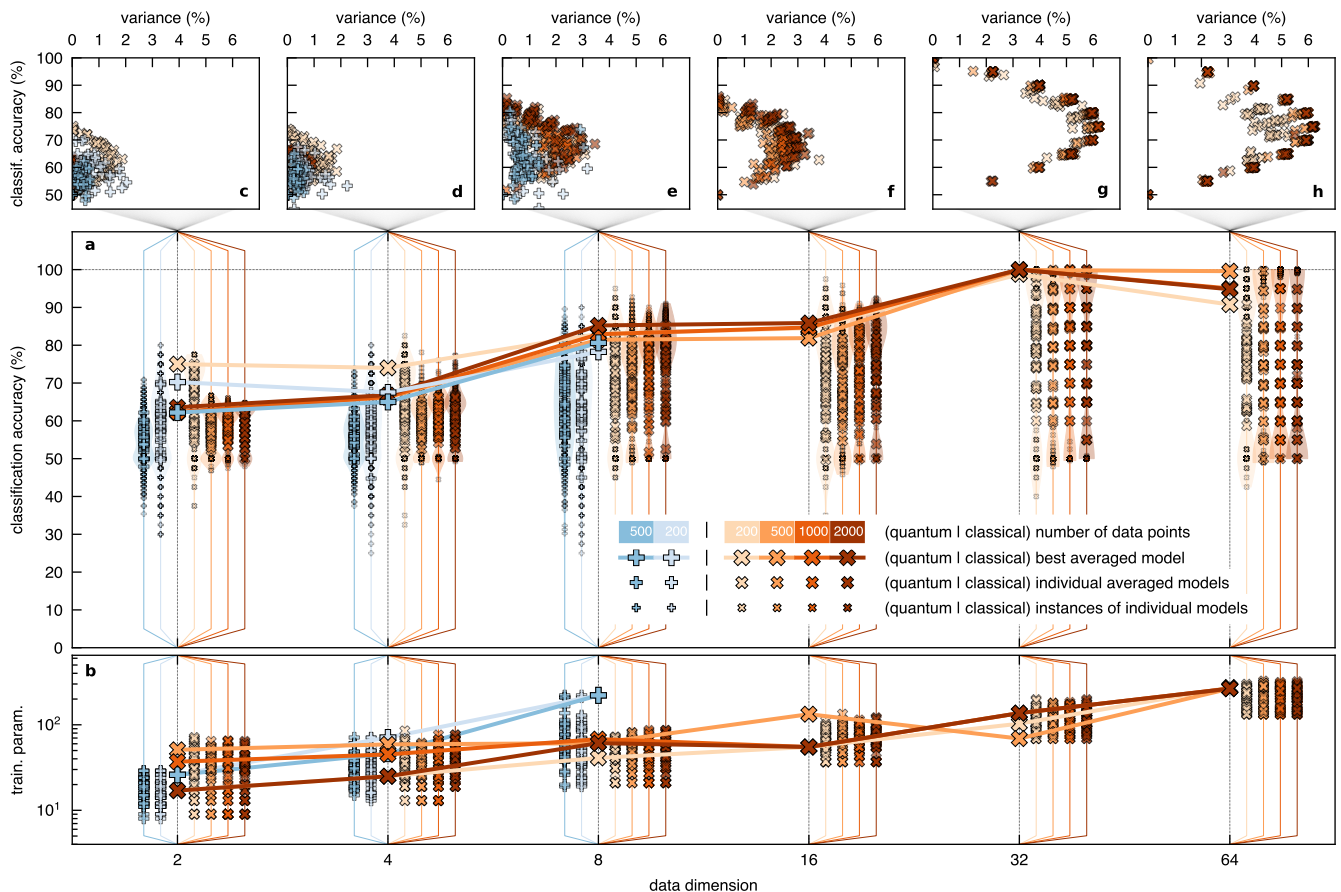


FIG. 4. Results for the third data set, i.e., the industrial image snippets from laser cutting machines, using a PCA for dimensionality reduction. Panel (a) shows the performance of 50 random classical (orange tones) and quantum (blue tones) neural networks for different data dimensions, i.e., sizes of data reduction, and data set sizes, ranging from 200 to 2000 data points split into training and validation data with a ratio of 80% to 20%. The medium sized markers show the 50 average performances of each of these 50 random models where the average is taken with respect to the outcome from training with 10 sets of random initial parameters, cf. Sec. III. The outcome from each of these sets is depicted by the smallest markers. The largest markers, connected additionally by a line for better visibility, indicate the performance of the best of the 50 random models. Panel (b) shows the corresponding number of trainable parameters for each model with those connected by a solid line reflecting the best performing models from panel (a). Panels (c)-(h) illustrate the different variances of the 50 random models with respect to the 10 resulting accuracies obtained from the 10 sets of random initial parameters.

them best for $d = 2$ and $N = 500$ ³. The corresponding classical neural network architecture is illustrated directly below Fig. 1 (i). Upon moving towards data reductions up to $d = 16$, we observe an increase in the best model’s averaged classification accuracies to roughly 80%, despite none of the individual runs with one set of initial training parameters ever reaching 100%. For $d = 32$ and beyond, our randomization approach starts yielding models giving rise to averaged classification accuracies up to 100%,

indicating that a reduction to $d = 32$ seems to capture enough information to warrant excellent classification.

Quantum models — The various blue colors in Fig. 4 (a) show the classification results for the 50 randomly generated quantum neural networks. Due to their demanding computational cost for simulating and training them on classical computers, we only generate networks that classify the data up to dimension $d = 8$ and for data sets with $N \in \{200, 500\}$. We observe that the maximally achieved classification accuracies are mostly similar to those achieved by the 50 randomly generated classical neural networks. At maximum, we observe averaged classification accuracies of $\sim 70\%$ for $d = 2$ and of $\sim 80\%$ for $d = 8$ for the best quantum models. The comparable performance of classical and quantum models is despite the fact that many of the quantum models perform on average worse than their classical counterparts. This is

³ Note that the best performance of $\sim 75\%$, as mentioned earlier, refers to the averaged classification accuracies of the best model and $N = 200$. This should not be confused with the visual representation in Fig. 1 (i), which corresponds to the best individual performance from among all 10 sets of initial training results of the best averaged model and is moreover for $N = 500$

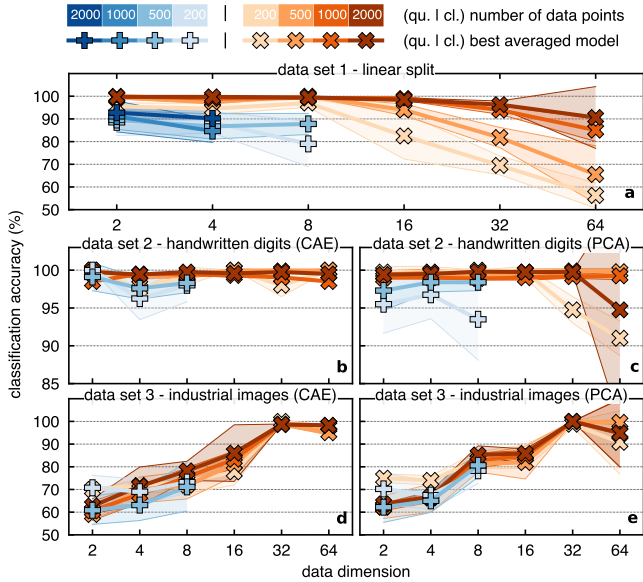


FIG. 5. Performance comparison between classical and quantum neural networks in terms of the classification accuracy of the best random models, i.e., the connected lines of Fig. 4 (a) but for all data sets. The shaded background indicates the standard deviation generated by the 10 individual random initial parameter sets that make up the shown averaged best random model performance.

indicated by the violin shapes in Fig. 4 (a), which indicate the bulk of the models’ performances. Similar to Fig. 1 (i), which exemplarily shows the learned function of the best performing classical neural network for $d = 2$ and $N = 500$, Fig. 1 (n) shows the same results for the best performing quantum neural network. The latter is illustrated directly above Fig. 1 (n). By comparing Figs. 1 (i) and (n), it is evident that despite the underlying data’s complexity, the classical model seems to approximate a rather simple function compared to the significantly more complicated one chosen by the quantum model. In addition, Fig. 4 (b) shows the number of trainable parameters for both classical and quantum models and confirms that both architectures have roughly similar numbers⁴. Figure 4 (b) also reveals that especially for the quantum models, the ones with the largest number of trainable parameters tend to perform best.

Variances — In Fig. 4 (c)-(h), we additionally analyze the variances of the classification accuracies given the 10 sets of random initial training parameters whose after-training performance on the validation data set defines the averaged classification accuracies shown in Fig. 4 (a). It can be seen that when comparing results of classical and quantum models with similar averaged classification accuracies, their corresponding variances differ slightly.

In fact, the quantum model variances seem to be generally smaller than those of the classical models. This is especially evident in Fig. 4 (e). Thus, although the quantum neural networks perform similarly at maximum but worse on average than their classical counterparts in terms of classification accuracies, they yield those results more consistently and do depend less on the initial starting parameters used for training. While a deeper statistical analysis is needed to confirm the generality of this property, this can be advantageous if good initial training parameters are not known in advance.

Moreover, we generally observe an increase in the accuracy variance of classical models as we increase the number of data points in the data set. This can be due to the additional data points increasing the separation hardness between the classes and leading to more complex loss landscapes. While the same was not observed for quantum models, this effect is clearer with higher data dimensions, where we lack information about the performance of the latter due to the high computational cost. Therefore, a deeper analysis would be needed for a fair comparison but it might be an explanation for the surprisingly good performance of the quantum model with $N = 200$ and $d = 2$ in Fig. 4 (a).

2. Summarized discussion of the remaining data sets

So far, we have discussed the classification results for the various versions of the third data set under a reduction via PCA. For the first and second data sets, cf. Secs. II A and II B, as well as the third one with CAE reduction, we summarize their main results in Fig. 5 (a)-(d). The various panels show exclusively the maximally achieved classification accuracies, from among the 50 randomly generated classical and quantum neural networks, obtained on the validation data set after training on the training data set. We deem this the most crucial performance indicator for comparing classical and quantum models.

For the third data set with CAE as the dimensionality reduction method, we give the results in Fig. 5 (d). In fact, they look very similar to those presented in Fig. 4 in almost every aspect. Most prominently, they also confirm that the best classical and quantum models perform equally well despite the overall difficulty to classify the strongly dimensionality-reduced industrial images. All classical and quantum model performances lie furthermore within one standard deviation of each other, thereby statistically confirming that none outperforms the other.

In the following, we discuss the results of the simpler first and second data sets. We are aware that classical linear classifiers should work well for these simple problems and the usage of classical neural networks seems unnecessary. However, since we require classical models for which we can argue a similar complexity to the quantum models analyzed, and in order to ease direct comparison, we opted for classical neural networks even for these easier tasks.

⁴ An exact equivalence is not possible due to the underlying randomization scheme in generating the models

In Fig. 5 (a), the results for the first data set, i.e., the linear split of the hypercube, are shown. While each version of the data set, distinguished by the number of data points N , achieves almost 100% classification accuracies for classical models and small hypercube dimensions d , their accuracies fall for larger d . This effect is even stronger for data sets with fewer data points, which is explainable given the hypercube’s growing size but constant number of sampling points from which to learn the function that splits it. In contrast, the best quantum models achieve classification accuracies of $\sim 90\%$ at maximum while their average and lowest performances (data not shown) show inferior performance compared to classical models as well. Moreover, not even the best models’ standard deviation reaches that of the classical models. This observation of inferior performance is in agreement with Ref. [16], which observed that a linear split through a hypercube seems to be surprisingly difficult to classify for quantum models. Nevertheless, by confirming former observations, we consider this a validation of our methodology.

In Fig. 5 (b), the results for the images of handwritten digits, dimensionality-reduced by a CAE, are shown. While each version of the data set, distinguished by their reduced dimension d and the number of data points N , achieves at least a classification accuracy of $> 95\%$ for both classical and quantum models, the accuracies for the quantum models are still slightly lower. This becomes even more pronounced when using a PCA instead of a CAE for dimensionality reduction with the corresponding results shown in Fig. 5 (c), although their standard deviations stay in touch with those of the classical models. However, given the simplicity of the classification task that originates from the simplicity of the corresponding dimensionality reduced data, cf. Fig. 1 (a) and (b), it is not surprising that both classical and quantum models solve the task well. This is in line with other studies targeting the same data set and which report similar classification accuracies [49, 50]. This serves as another validation of our methodology.

3. Examination of learned functions and variances

At last, we want to exemplarily compare the learned functions of the best performing classical and quantum neural networks for all three data sets and both reduction methods to $d = 2$, which is unfortunately the only dimension for which we can visualize them. The results are shown in Fig. 1 (f)-(j) and (k)-(o) for classical and quantum models, respectively, and the corresponding best performing model architectures are shown directly below or above the panels, respectively. We observe across all data sets that the quantum models tend to learn more complex functions than the classical ones despite some of the data’s simplicity, especially for the first and second data sets. Note that the classically learned functions do not change qualitatively or in simplicity even if replacing the linear activation function $\text{ReLU}(x) = \max(0, x)$ with

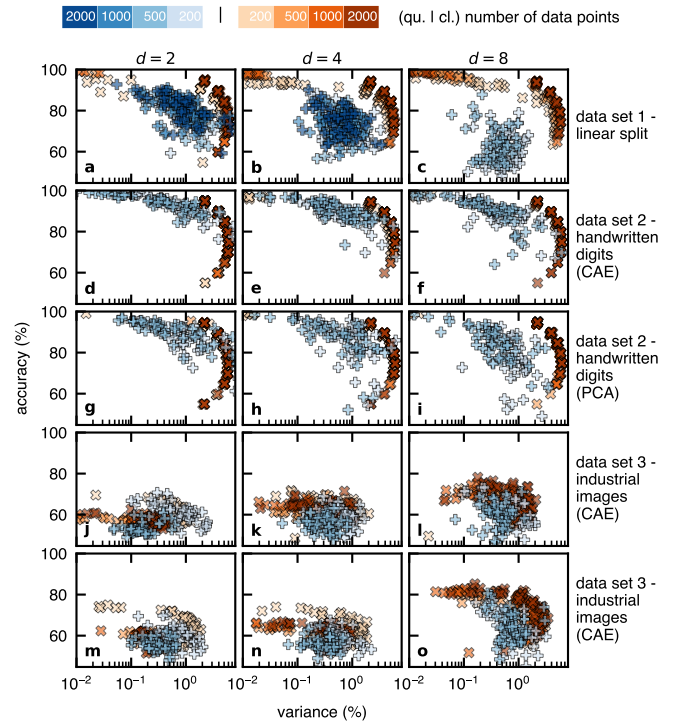


FIG. 6. Overview of the variances as shown in Fig. 4 (c)-(h) but for all data sets and reduction methods as indicated on the right-hand side of each row. We only show it for those data dimensions d for which we have results for both classical and quantum neural networks.

a non-linear one like $\tanh(x)$ (data not shown). Following from Ref. [51], this may help evaluate if the considered quantum neural networks have a poor inductive bias. Moreover, we also want to stress that we observe the same behavior of the variances as discussed in Fig. 4 (c)-(h). We provide an overview of the variances with respect to the other data sets and reduction methods in Fig. 6. In fact, the effect of the quantum models generally having lower variance with respect to the starting parameters is even stronger for the first and second data sets. Hence, this observation holds for all examined data sets.

4. Comparison with literature quantum models

As a means to compare our randomized quantum neural networks to known quantum models, we additionally benchmark the performance of three literature models, namely Chebyshev [52], Hubregtsen [40] and HighDim [53]. To this end, we apply them to each data set and evaluate their performance as the averaged classification accuracy obtained from training with 10 sets of initial parameters. The comparison between our randomized quantum neural networks and these models (data not shown) yields that our best randomized models perform on par or even better than these specific literature models, with Hubregtsen showing the best performance. This holds for all data

sets.

B. Analysis of correlations between performance and hyperparameters

We now analyze whether there are some common features which distinguish well and badly performing random models. To this end, we first investigate the correlation between the achieved classification accuracies and the total number of trainable parameters in the model, since the latter is often connected to a model’s expressivity and thus performance. Figure 7 (a) analyzes this correlation for the first data set and reveals that the classification accuracy of the hypercube data for $d = 2$ does not depend much on the number of trainable parameters, as low and high accuracies can be observed for both low and high numbers of trainable parameters. This changes for higher dimensional hypercubes, which show an increasing correlation between accuracy and the number of trainable parameters when moving to $d = 4$ and then further to $d = 8$. This behavior is even stronger for the two versions of the third data set of industrial images, distinguished by the employed reduction method and shown in Fig. 7 (d) and (e). A possible explanation would be that due to the increased complexity of the data, cf. Fig. 1 (d) and (e), it takes more parameters to express a sufficiently complex function that is able to at least partially approximate the exact but unknown classification function $f : \mathbb{R}^d \rightarrow \{0, 1\}$. This is also in line with the results for the second data set presented in Fig. 7 (b) and (c), where the number of trainable parameters seems to play the least important role compared to the other two data sets. This is explainable by the underlying data’s low complexity, cf. Fig. 1 (a) and (b). Interestingly, we find that the correlations in Fig. 7 (a), (d) and (e) originate mainly from correlations between the classification accuracy and the number of trainable parameters in the PQC $U_{\text{pqc}}(\mathbf{x}_i, \phi, \theta)$ and not so much due to correlations with the number of trainable parameters in the measurement operator $O(\omega)$. If explicitly calculating the correlations statistics with respect to either of the two (data not shown), we find very similar statistics to that shown in Fig. 7 (a)-(e) for the PQC and observe no correlations for the measurement operator.

Since the total number of trainable parameters is intimately connected to the number $n_{\text{layer},q}$ of layers in $U_{\text{pqc}}(\mathbf{x}_i, \phi, \theta)$, we analyze its correlation with the classification accuracies in Fig. 7 (f)-(j). Interestingly, its correlation is not as strong as expected for none of the data sets, despite their observed correlation with the number of trainable parameters in Fig. 7 (a), (d) and (e). We do, however, observe an increase in the average classification accuracies across all data sets and all data dimension when using two layers instead of one. For $n_{\text{layer},q} > 2$, the results are again rather mixed with the classification accuracies stagnating for the first and second data set. For the third data set, we still see a slight increase in classification accuracies up to $n_{\text{layer},q} = 4$. However,

the general observation that $n_{\text{layer},q}$ does not seem to be crucial when predicting a randomized quantum neural network’s performance is also in line with similar results observed in our brief comparison with literature models

Next, we examine the correlation between the classification accuracy and the number of entangling gates in the PQC — if the model’s randomized generation adds any in the first place. While Fig. 7 (k)-(o) seem to indicate a substantial correlation between the two quantities, we also do not want to over-interpret the results. In our randomized models, each entangling gate comes with a trainable parameter. Hence, having entangling gates or not heavily impacts the number of trainable parameters and the observed correlation might therefore be a reflection of Fig. 7 (a)-(e) or vice versa. A potentially more insightful quantity to calculate when analyzing the necessity or impact of entangling gates, respectively entanglement, is shown in Fig. 7 (p)-(t). There, we calculate the entangling power of all entangling gates using the gate concurrence [54] for every gate’s final training parameter. It is a measure $\mathcal{C}(U) \in [0, 1]$ for all two-qubit gates $U \in U(4)$ and attains 0 (1) if the corresponding gate U is non-entangling (maximal entangling). We do not find a correlation between a model’s classification accuracy and the model’s averaged gate entangling power

$$\bar{\mathcal{C}} = \frac{1}{N_{2q}} \sum_{i=1}^{N_{2q}} \mathcal{C}(U_{i,\text{trained}}), \quad (18)$$

with i running over all N_{2q} trained entangling gates $U_{i,\text{trained}} \in U(4)$ present in the model’s PQC. The same holds if analyzing the averaged change in gate entanglement power (data not shown), which is given by

$$\bar{\mathcal{C}}_{\text{change}} = \frac{1}{N_{2q}} \sum_{i=1}^{N_{2q}} [\mathcal{C}(U_{i,\text{trained}}) - \mathcal{C}(U_{i,\text{init}})], \quad (19)$$

with $U_{i,\text{init}}$ the untrained version of $U_{i,\text{trained}}$ determined by the initial training parameters. This analysis reveals that high classification accuracies are neither correlated with larger gate entanglement powers nor with the optimizer increasing it during training. This highlights the highly non-trivial effect that entanglement has on a model’s performance. While having entangling gates seems to be mostly beneficial, they are not necessarily required for their entanglement-generating properties.

Besides the correlations analyzed in Fig. 7, we also analyze the correlations between the classification accuracy and various other quantities (data not shown), for instance with respect to the number of qubits n_q , the form of the measurement operator $O(\omega)$, the form of the entangling structure or the employed feature encoding. We did not find any correlations for any of these quantities for any of the data sets. We therefore conclude that our correlation analysis in general does not yield any clear indicator or rule on how most of the varied hyperparameters of the random quantum neural networks should be chosen for ideal performance. The only deducible rule seems to be

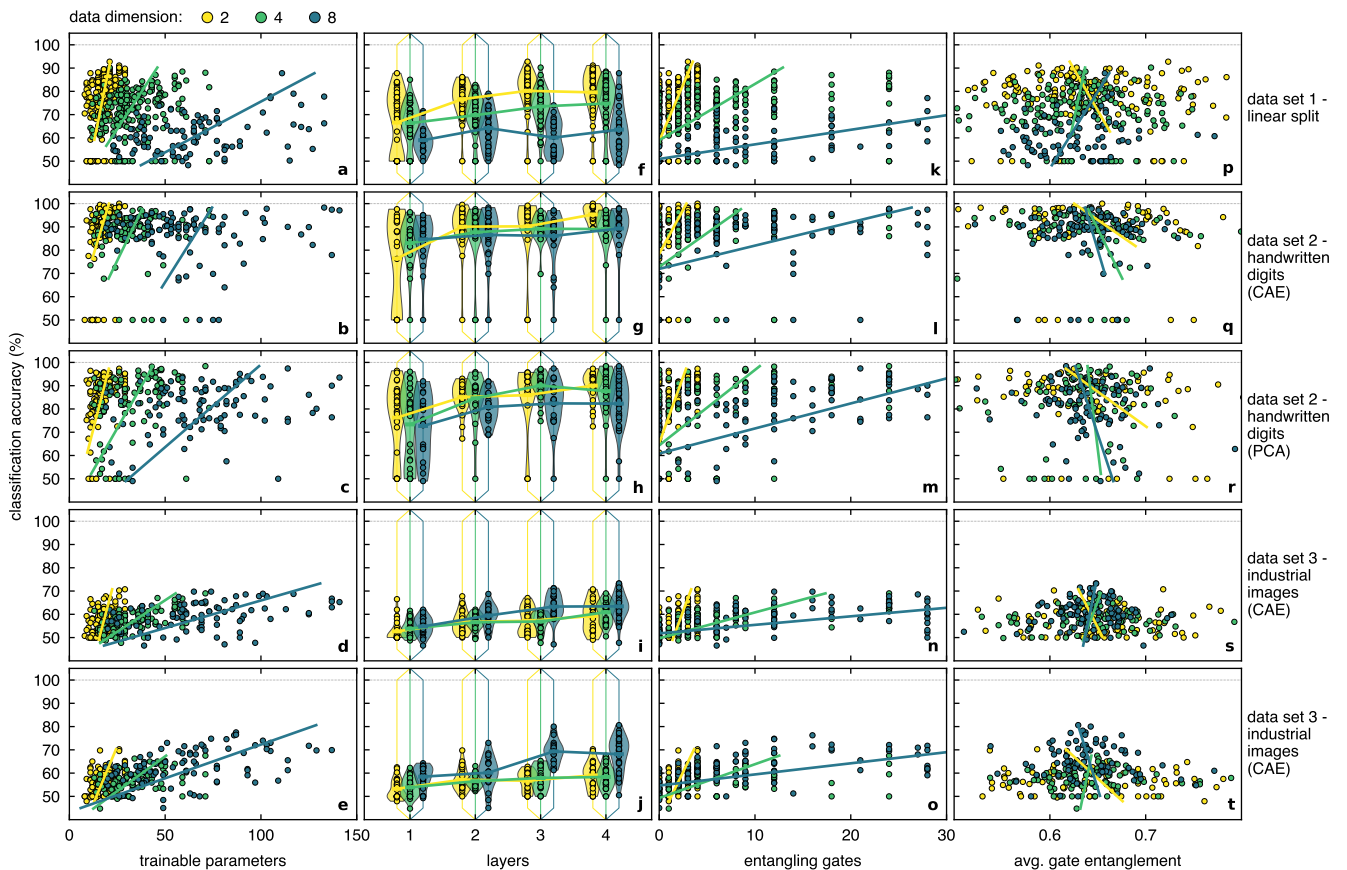


FIG. 7. Correlation analysis for the 50 random quantum neural networks in terms of correlations between classification accuracy and various properties of the parametrized quantum circuit. The five rows correspond to the results obtained for the five data sets as indicated on the right. For simplicity and in order to have more data points for each data set, we merge all versions of each data set. To be precise, this implies that the presented data for the first data set contains the results gathered independently from training results with $N \in \{200, 500, 1000, 2000\}$ data points. For the second and third data set, it implies joining results gathered independently by training them with $N \in \{200, 500\}$. The colors distinguish the data dimensions. In panels (a)-(e), the correlation between the joint number of trainable parameters in the PQC $U_{\text{pqc}}(\mathbf{x}_i, \phi, \theta)$, cf. Eqs. (5) and (6), as well as its measurement operator $O(\omega)$, cf. Eqs. (8a) and (8b), and the classification accuracy is analyzed. In panels (f)-(j), the correlation between the number $n_{\text{layer},q}$ of layers in the PQC and the classification accuracy is analyzed. While panels (k)-(o) analyze the correlation between the number N_{2q} of entangling gates and the classification accuracy, panels (p)-(t) analyze how their averaged gate entangling power, measured by Eq. (18), for the trained model is correlated with the accuracy. The linear lines in every panel — except panels (f)-(j) — solely indicate the general trend of the corresponding data and should not be taken as a fit to the data. Note that we do not take models yielding exactly 50% classification accuracy after training into account for calculating the trend lines as those models are intrinsically untrainable, due to bad luck during randomization, and would otherwise impact the trend for actually trainable models.

that having more trainable parameters in the quantum models is almost always beneficial at the tested problem scale, and irrelevant at worst.

However, we may deduce something when analyzing only the best-performing quantum models. Upon inspecting in detail the structure of the three best-performing quantum models for all combinations of data set, dimensionality reduction method and number of features, we report that only five out of these 90 models were circuits without any entangling gates. Moreover, analyzing the cases where we have $d = 8$ features per data point, only three out of the 30 best models did not use all-to-all entanglement. For these specific cases in particular, the

best-performing quantum model always used all-to-all entanglement.

C. Comparison of quantum model performances across data sets

We now utilize the fact that we have classification results for various randomly generated quantum neural networks on various data sets. This allows a cross-data set comparison of model performances in the sense that we can compare whether models which perform well on one particular data set also perform well on other data sets.

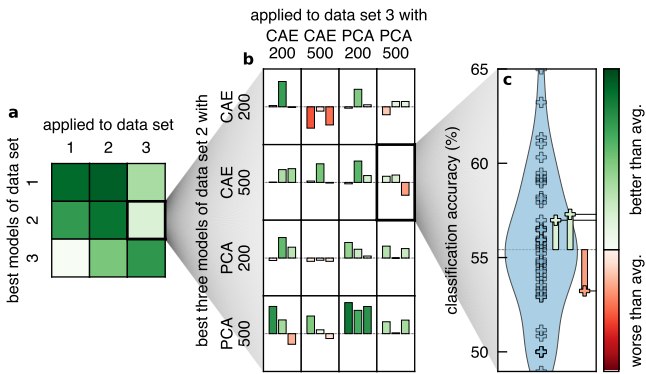


FIG. 8. Cross-comparison of quantum neural network performances between different data sets. Panel (a) shows the color-coded averaged model performance when applying the best three quantum models of each data set to itself and each of the other data sets. Panel (b) exemplifies the averaging process by showcasing the individual results that are being averaged and shown in panel (a). In detail, panel (b) shows the results when taking the three best performing models from each version of the second data set, i.e., either $N = 200$ or $N = 500$ data points and either CAE or PCA as dimensionality reduction method, and applying each of them to each version of the third data set, i.e., again using either $N = 200$ or $N = 500$ data points and either CAE or PCA as dimensionality reduction method. Panel (c) illustrates the color code used in panels (a) and (b) exemplarily. The greener [redder] the tile in panel (a) or bars in panel (b), the higher above [lower below] the three best models from the original data set (data set 2, CAE reduction, 500 data points in panel (c)) perform with respect to the average random model’s performance on the new data set (data set 3, PCA reduction, 500 data points in panel (c)). This is also illustrated by the non-linear colorbar on the right of panel (c), whose maximum/minimum/center is aligned with the best/worst/average performances given by the 50 random quantum neural networks generated for the new data set (data set 3, PCA reduction, 500 data points). All data sets have dimensionality $d = 4$.

This way we may assess whether some of the randomly generated models seem to be well-performing in general. To this end, Fig. 8 (a) shows the cross-data set performances of the best performing models from one data set when applied to any of the other data sets. However, in order to have enough statistical data to average over, we always take the best three models — quantified by the three highest classification accuracies — and train them on other data sets. Moreover, in Fig. 8 (a), we also average over the different versions of each data set, i.e., we average over the results when applying the best three models for one particular version of a data set to one particular version of another data set. The different versions are distinguished by their number of data points or the employed reduction method in the case of the second and third data sets. The data dimensionality is kept identical to allow a model’s applicability to a different data set. It is exclusively $d = 4$ for Fig. 8. Figure 8 (b) shows in detail how the results of Fig. 8 (a) are obtained for the example

of applying the best models of the second data set to the third data set. The various panels in Fig. 8 (b) show the results when using the best three models for each of the four versions of the second data set, distinguished by $N \in \{200, 500\}$ and CAE or PCA as reduction method, to the same four versions but of the third data set. For one of the panels in Fig. 8 (b), we show how its cross-data set performance is calculated in Fig. 8 (c). In the chosen example, this implies how the best three models for the second data set with $N = 500$ data points and CAE as reduction method (called original data set in the following) perform when trained for the third data set with $N = 500$ data points and a PCA reduction (called new data set in the following). The three model performances — evaluated again by averaging each model’s results for 10 set of random initial training parameters — are then compared to the best, average and worst performances of the 50 random quantum models previously generated for the new data set. A model from the original data set is considered good (bad) if it performs better (worse) than the average performance of the new data set. This is indicated with green (red) bars in Fig. 8 (c). The colors of these bars carry the relevant information in Fig. 8 (b) and their average determines the results presented in Fig. 8 (a).

With this explanation in mind, we may discuss Fig. 8 (a) and first observe that every model which performs well on any of the three data sets also performs well on the second data set, which we attribute to the latter data set’s simplicity. The contrary, however, is not true. The models which perform well on the first and second data sets seem to perform rather mediocly on the third one, and the best performing models on the third data set perform likewise mediocly on the first data set. This separation seems to be correlated with the data’s complexity, cf. Fig. 1 (a)-(e), specifically with how separable the two classes are. While the first and second data sets are rather simple, in the sense that they are almost always linearly separable, the third data set is more complex and the classes are never linearly separable. We thus conclude that, while our randomized generation of quantum neural networks seems to yield decent models which perform mostly well, and at worst mediocly on all tested data sets, in order to have the best possible performance, customized models need to be crafted in a data-set-dependent way.

V. RESULTS FROM CONVOLUTIONAL NEURAL NETWORKS

After the discussion of the classification results of the dimensionality reduced data sets from Sec. II in the previous Sec. IV employing the first methodology, cf. Sec. III A, we now turn towards presenting the results employing the second methodology, cf. Sec. III B, to classify the original, non-reduced image data.

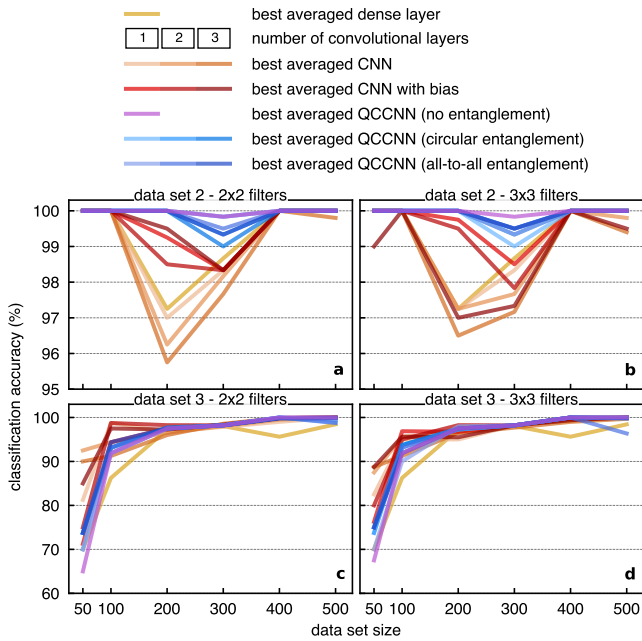


FIG. 9. Performance comparison between fully-classical (warm colors) and quantum-classical hybrid (cool colors) convolutional neural networks (CNN and QCCNN, respectively) in terms of the classification accuracies of each tested model as function of data set size N , for both non-reduced image data sets, cf. Secs. II B and II C. A quantum model is determined by a particular choice of three hyperparameters: size of the quantum-convolution filter, entanglement structure in the quantum circuit used in the quantum convolution, and number of layers in this quantum circuit. The performance of a single dense classical layer with two neurons and softmax activation function is given as baseline (golden line). The data is also separated by the size of the (quantum) convolution filter such as to not overcrowd each plot.

A. Comparison of classical and hybrid convolutional neural network performances

Similar to the previous analysis of the dimensionality reduced data sets, we start our analysis for the non-reduced data sets by comparing the performance in terms of classification accuracies for the fully-classical and quantum-classical hybrid scheme — here given by CNNs and QCCNNs, respectively. However, while running the first simulations for the handwritten-digit data sets with $N = 200$ and $N = 500$ images, we noticed a large discrepancy between the classification accuracy of CNNs and QCCNNs for the $N = 200$ data set, in favor of the latter models. This discrepancy could not be observed for the data set with $N = 500$. To study this possible advantage in few-data scenarios in more depth, we decided to generate more data sets with various N , following the same generating principles as described in Sec. II. In the following, we apply our (quantum) convolutional models to data sets with size $N \in \{50, 100, 200, 300, 400, 500\}$.

In Fig. 9, we summarize the results obtained with all

tested models, in terms of classification accuracies on the validation data sets as a function of the data set size N . The handwritten-digit data sets are shown in panels (a) and (b) and the industrial-image data sets in panels (c) and (d). As before, the classical models are depicted as warm-color lines, while the hybrid models as cool-color lines.

1. Discussion of data set 2 — handwritten digits

For the handwritten-digit data sets, QCCNNs consistently reach classification accuracies close to 100%, while CNNs achieve as low as 96% for some data set sizes. Interestingly, QCCNNs without entangling gates show the best performance (purple lines), which indicates that this advantage is most likely not due to inherently quantum mechanical properties, but probably due to the algorithmic structure, which might even be efficiently classically simulable. Moreover, the initial assumption of quantum advantage in few data scenarios is not confirmed. In fact, for the smallest data set size, all classical and hybrid models achieve 100% accuracy. This confirms that, in this regime of very few data, the choice of individual images has a large impact in defining the problem hardness.

2. Discussion of data set 3 — industrial images

For the industrial-image data sets, the performances of fully-classical and quantum-classical hybrid models are very similar, with the former showing better generalization ability for the smallest-sized data sets of $N = 50$ and $N = 100$ images. For these data sets, QCCNNs with entangling gates perform slightly better than those without. However, for the larger-sized data sets, both CNNs and QCCNNs, as well as all tested varieties of the latter, perform almost identically. We highlight that, even for the most challenging data set, QCCNNs show averaged accuracies below 95% only for data sets with $N \in \{50, 100\}$. On the one hand, this indicates that these models are already expressive enough to deal with some industry-relevant use cases. On the other hand, the considered industrial images may still not exhibit enough complexity to fully benchmark these models, thus preventing us from drawing more rigorous conclusions.

For both data sets, similar arguments can be made when analyzing the best averaged model's cross entropy loss values on the validation data sets (data not shown). We note that, despite QCCNNs without entangling gates achieving a similar performance to QCCNNs with entangling gates, the former took more iterations to converge both in classification accuracy and cross-entropy loss in most scenarios (data not shown). However, this effect was more apparent for the scenarios with smaller-sized data sets. We further highlight that, for the handwritten-digit data sets, while most classical and hybrid models con-

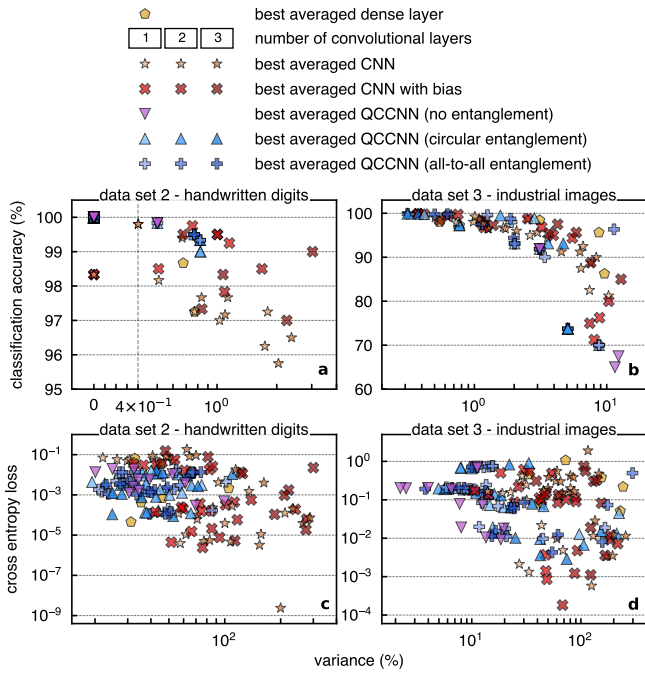


FIG. 10. Correlation analysis for the CNNs (warm colors) and QCCNNs (cool colors) in terms of correlations between classification accuracy [cross entropy loss] on the validation data sets and its variance, for both image data sets. The accuracy [loss] analysis can be seen in panels (a) and (b) [(c) and (d)]. For simplicity and to have more points for each data set, each panel contains results for models with all sizes of (quantum) convolution filter, each trained with $N \in \{50, 100, 200, 300, 400, 500\}$ data points. The performance of a single dense classical layer with two neurons and softmax activation function is also analyzed for comparison (golden pentagons). In order to represent points with null variance, the variance axis in panel (a) has a symmetrical logarithmic scale where the range $[0, 4 \times 10^{-1}]$ is linear and $[4 \times 10^{-1}, \infty)$ is logarithmic. A vertical dashed line separates these two ranges for clarity.

verged in validation accuracy within the 100 epochs, some did not. This encompasses in particular the QCCNN with a 3×3 quantum convolution filter and without entangling gates for $N = 300$, as well as multiple CNNs for $N = 200$. On the other hand, for the industrial-image data sets, some models did not converge within the 100 epochs, specially for the smaller data sets with $N \in \{50, 100\}$, indicating that higher accuracies than the ones displayed may in general be achievable with these models.

3. Examination of performance variances

Figure 10 (a) and (b) show the relationship between the models' performance metrics and their variance across the 10 runs with different initial parameter sets, for both image data sets. The same color structure as in Fig. 9 encodes the results. For simplicity and to maximize the

number of points available for the analysis, each panel contains results for models with all sizes of (quantum) convolution filters, trained with each data set size. On average, QCCNNs show lower performance variance than CNNs, which agrees with our observation for random neural networks, cf. Fig. 4 (c)-(h). This lower variance of models with quantum-circuit components can be seen even clearer when analyzing the relationship between the classification accuracies' variance and the underlying cross-entropy loss shown in Fig. 10 (c) and (d) for each data set.

We observe a negative correlation between classification accuracy and its variance, cf. Fig. 10 (a) and (b), which may be interpreted as better-performing models having a loss landscape whose better-performing minima are more easily reachable independently of the initial parameters. In particular, all models achieving an accuracy of 100% for the handwritten-digit data sets show no accuracy variance. Thus, their performance was completely independent of the chosen initial parameters.

B. Analysis of correlations between performance and hyperparameters

We now perform the same analysis we did for the random quantum neural networks, cf. Sec. IV B, in terms of classification accuracy and various properties of the quantum circuits used in the QCCNNs, in order to identify key ingredients of either well or badly performing models. Figure 11 shows some of the analyzed properties of the quantum circuits of all QCCNNs used, for each data set and each trained with all data set sizes available, in order to maximize the number of points available for the analysis. Visually, we opt to separate by color the entanglement structures of the circuit used for the quantum convolution and the number of layers in this quantum circuit. However, we consider all data points when looking for any correlations or interesting patterns. Since, for each data set type, the number of trainable parameters in the final dense classical layer of each QCCNN is similar, changing only if the images need padding before the quantum convolution, we opt to analyze the correlation between the achieved classification accuracy and the number of trainable parameters in the quantum circuit of the quantum convolution. This is represented in Fig. 11 (a) and (b), for the data sets indicated on the right. The accuracy does not seem to depend on the number of trainable parameters in the quantum circuits, since there are both well and badly performing models with both few and many trainable parameters in the quantum layer. However, the amount of data is too limited to draw a statistically significant conclusion from this.

Looking at Fig. 11 (c) and (d), which show the relationship between accuracy and the number of layers in the quantum circuit of the QCCNN, we also find no clear correlations. This is in line with the observations made for random quantum neural networks, cf. Fig. 7 (f)-(j).

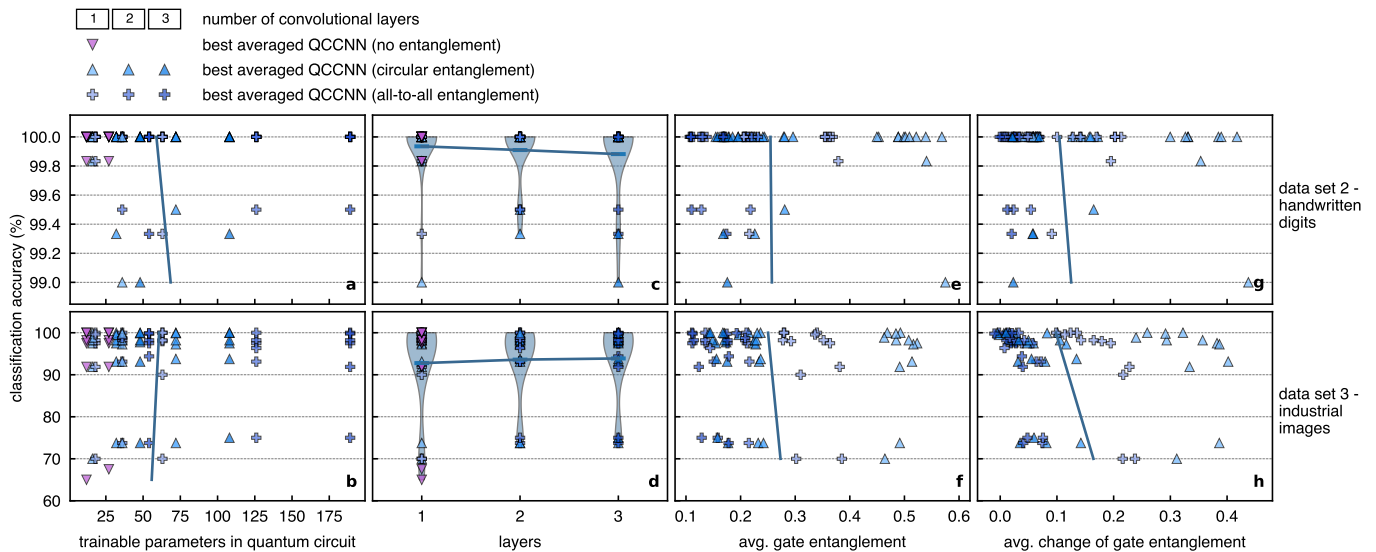


FIG. 11. Correlation analysis for the quantum-classical hybrid convolutional neural networks (QCCNN) in terms of correlations between classification accuracies and various properties of the parametrized quantum circuit used for the quantum convolution. Each row corresponds to the results obtained for the data set indicated on the right. For simplicity and to have more points for each data set, we merge all QCCNNs and data set sizes used. Therefore, each panel contains results for models with all sizes of quantum-convolution filter, all entanglement structures of the circuits used for its quantum convolution, and number of layers in this quantum circuit, each trained with $N \in \{50, 100, 200, 300, 400, 500\}$ data points. Visually, we still separate the latter two hyperparameters (entanglement structure and number of layers) by color. In panels (a) and (b), we analyze the correlation between classification accuracy and number of trainable parameters in the quantum circuit used in the quantum convolution. In panels (c) and (d), we analyze the correlation between classification accuracy and the number of layers in the quantum circuit. In panels (e) and (f), we analyze the correlation between classification accuracy and averaged gate entangling power \bar{C} , cf. Eq. (18), of the models after training. Finally, panels (g) and (h) analyze the correlation between classification accuracy and the change of this average gate entanglement power before and after training, cf. Eq. (19). The QCCNNs without entangling gates are omitted in panels (e)-(h). The linear lines in every panel — except panels (c) and (d) — solely show the general trend of all the data and should not be taken as a fit to the data. In panels (c) and (d), the lines connect the average accuracy of each set of QCCNNs with a specific number of layers in its quantum circuit.

It is again hard to extract more rigorous conclusions, especially because the median accuracy for each set of QCCNNs with a specific number of layers in its quantum circuit is always very close to 100%.

Since the entangling gate structures were fixed and all entangling gates parametrized, the correlation between the number of trainable parameters and the number of entangling gates is very high, by definition. Therefore, we opt not to show this correlation plot. To analyze the usefulness of entanglement in QCCNN models, we calculate the averaged gate entangling power \bar{C} , cf. Eq. (18), of the models after training, as done in Sec. IV B. For this analysis, we exclude QCCNNs without entangling gates for obvious reasons. The relationship between this metric and classification accuracy is shown in Fig. 11 (e) and (f), for each data set. We do not find a correlation between the classification accuracy of a QCCNN and its averaged gate entangling power \bar{C} . However, for the handwritten-digit data set, we observe that most models with larger \bar{C} reach a classification accuracy of $\sim 100\%$ on

the validation data set. Conversely, if a model performs badly, it is most likely one with lower \bar{C} . Nevertheless, the amount of data is again too limited to make a statistically significant statement. We still note that QCCNNs with more entangling gates show a lower \bar{C} , which we further analyze in Fig. 12. In fact, these two quantities seem to be inversely proportional. Fitting the expression

$$\bar{C}(N_{2q}) = \frac{a}{N_{2q}} + b, \quad (20)$$

with N_{2q} the number of entangling gates in the quantum circuit used for the quantum convolution, to all data points, we get the curve depicted in Fig. 12, with parameters $a = 1.47 \pm 0.10$ and $b = 0.13 \pm 0.01$. We may explain this inverse relation as a consequence of the total gate entangling power being distributed among all entangling gates for each model.

This inverse relationship raises a fundamental question about what metrics really capture the utility of entanglement in quantum models. There is certainly nuance between: (i) the binary metric of presence or absence of

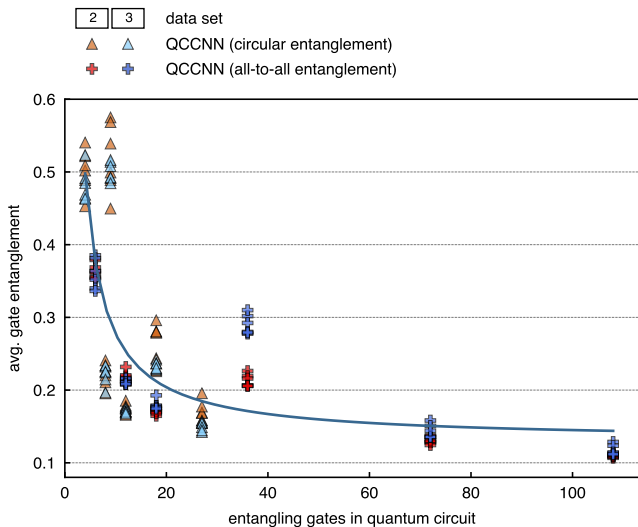


FIG. 12. Averaged gate entangling power \bar{C} , cf. Eq. (18), of QCCNNs with entangling gates, after training, as a function of the number N_{2q} of entangling gates in the quantum circuit used for the quantum convolution. The data points of both Fig. 11 (e) and (f) are shown here. Data points of QCCNNs trained with the handwritten-digit data sets have warm colors, while those trained with the industrial-image data sets have cool colors. QCCNNs with circular entanglement structure have lighter tones, while those with all-to-all entanglement have darker tones. The hyperbolic curve was fit to all the data points.

entangling gates, (ii) the discrete metric of number of entangling gates, and (iii) the continuous metric of gate entangling power. This inverse proportionality between the metrics (ii) and (iii) challenges the intuitive assumption that more entangling gates likely lead to more useful entanglement for machine-learning tasks — an assumption often made in the design of quantum circuits for machine learning. While a deeper analysis is needed, this suggests that, for problems which require a specific amount of entanglement generated by a quantum model, models with concentrated entanglement through fewer, more powerful gates may be as performant as models with entanglement distributed across many weaker gates. Thus, we suggest that practitioners should focus on optimizing gate entangling power rather than simply increasing the number of entangling gates in their studies. Moreover, training the former should be easier through classical simulation, since they can have many fewer parameters and, thus, require fewer circuit simulations to calculate gradients.

We perform the same analysis for the average change of gate entanglement power \bar{C}_{change} , cf. Eq. (19), during training, shown in Fig. 11 (g) and (h), for each data set. We also find no correlation between this metric and the classification accuracy. However, we note that, for both data sets, roughly 2/3 of the individual entangling gates across all QCCNNs increase their entangling power during training. Moreover, virtually all models show a

positive \bar{C}_{change} , with only five models out of 144 showing a slightly negative \bar{C}_{change} . While this seems like a positive argument for the use of entanglement as a resource in quantum machine learning, we must keep in mind that quantum-classical hybrid models without entangling gates performed similarly well as the ones with entangling gates, in most scenarios.

VI. SUMMARY AND CONCLUSIONS

In this study, we conduct a systematic investigation of classical- and quantum-machine-learning approaches for binary image classification across data sets of increasing complexity. Our work provides a uniquely comprehensive hyperparameter optimization analysis — rarely conducted in quantum-machine-learning literature — offering insights into which quantum circuit properties actually contribute to model performance. We evaluate both classical and quantum-classical hybrid approaches using three progressively complex data sets: (i) artificial hypercube data, (ii) MNIST handwritten digits (0’s and 1’s) [20], and (iii) industrial images of practical relevance from laser cutting machines.

Our methodological framework employs two complementary approaches: (1) randomized (quantum) neural networks applied to dimensionality-reduced data, and (2) (hybrid) convolutional neural networks applied to full image data. Both methodologies effectively compare fully-classical versus quantum-classical hybrid pipelines. Dimensionality reduction through convolutional autoencoders (CAE) and principal component analysis (PCA) serves as a necessary preprocessing step for fully-quantum models, as the high dimensionality of industrial data sets would otherwise make them computationally intractable for quantum processing. The first methodology employs either classical or quantum neural network classifiers on dimensionality-reduced data, while the second uses either classical CNNs or quantum-classical hybrid convolutional neural networks (QCCNNs) [21].

Quantitatively, using classification accuracy on validation data as our performance metric, we observe that classical and quantum methods achieve statistically equivalent classification accuracies across most tested data sets. For the industrial image data, maximum averaged accuracies of quantum models reached approximately 80% for dimensionality-reduced data with $d = 8$ features and between 95% and 100% for full-image classification with convolutional approaches, except for the smallest data sets containing 50 and 100 total images. Our results from the two simple data sets, the linear split of a d -dimensional hypercube and the 0’s and 1’s from MNIST’s handwritten images, are in good agreement with previous studies [16], confirming that MNIST is trivial for both classical and quantum models while, for the linearly-split hypercube, despite its simplicity, it is already surprisingly challenging to reach classification accuracies beyond 90%. However, these two simple data sets are merely used to benchmark

our methodologies and validate their application for the industry data set. This empirical equivalence in performance highlights a significant finding: despite substantial theoretical advancement in quantum machine learning, practical implementation on industrial data sets shows no clear practical advantage in classification accuracy. From an industry perspective, we do not observe quantum models to offer any practical advantage for the considered binary classification tasks and classical data sets. The most likely reason as to why we did not observe a practical advantage, if there is one to observe in the first place, is that we needed to restrict our quantum models to small and medium sizes in order to keep them simulable. This might change with more powerful quantum hardware that supports executing quantum models which reduce or fully avoid any classical processing.

An intriguing finding is that quantum and hybrid models demonstrate significantly lower variance in classification accuracies with respect to initial training parameters compared to classical approaches. This was consistently observed across all data sets and methodologies, suggesting improved stability in quantum models when optimal initialization parameters are unknown — a potentially valuable property for practical applications as it implies more predictable performance. Conversely, when analyzing learned decision boundaries, classical models consistently produced simpler functions while quantum models generated notably more complex classification boundaries, even for data sets with easily-separable classes. This tendency towards non-linear complexity despite no performance advantage may indicate a lack of appropriate regularization mechanisms which encourage simpler solutions — a simplicity bias, often beneficial for generalization — in the quantum models used [51]. The disconnect between our findings and approaches focused on inductive biases [47, 48] suggests that practical advantage may require careful design of quantum architectures, such that they are able to fully exploit known structures in the data, rather than relying on generic quantum properties.

Our comprehensive hyperparameter analysis revealed surprisingly few consistent correlations between model-architecture choices and performance. Among all parameters analyzed (feature encoding methods, number of circuit layers, entangling gate type and structure, gate entangling power, measurement operators), only the number of trainable parameters showed a consistent positive correlation with model performance. However, this is not a general statement as, at some point, we expect to run into the overfitting regime. The inconsistent importance of hyperparameters across our experiments — particularly regarding entanglement structure and gate entangling power — illuminates the current limited theoretical understanding of how quantum models actually function and what determines their performance.

For the randomized quantum neural networks, we found no correlation between model performance and total averaged gate entanglement power or its change during training, with gate entangling power quantified using gate

concurrence [54]. However, $\sim 94\%$ of the best performing models did feature entangling gates, often with all-to-all connectivity. Nevertheless, we note that this entanglement structure can always be mapped to a linear one with a polynomial gate overhead [55]. Thus, while the type of entangling structure may not be a crucial factor, the non-negligible entangling power of the top-performing models is a hopeful observation.

For QCCNNs, models without entangling gates performed equally well as those with entanglement in most scenarios, though they required more iterations to converge in both classification accuracy and cross-entropy loss, especially with limited training data. This suggests that, while entanglement may not be a crucial factor for the performance of quantum-classical hybrid models, it may still be beneficial for their training. Nevertheless, we must note that the QCCNNs tested here have significantly more classical training parameters than quantum ones. Thus, their expressive power is likely dominated by their final classical dense layer. Hence, the expressive power of the quantum convolutional layer might be too limited, irrespective of it having entangling gates or not. Interestingly, for the QCCNNs, we still observe a positive change in averaged gate entanglement power due to training in virtually all scenarios. Most importantly, we also observed an inverse relationship between the number of entangling gates and per-gate entanglement power, suggesting that the total entanglement capability is distributed among available gates — a finding with implications for efficient quantum circuit design.

While a deeper statistical analysis would be needed to confirm the generality of these properties, the entanglement findings in this study highlight a critical gap in our current understanding of quantum resource utilization. While we can measure various aspects of entanglement — from gate-level concurrence [54] to circuit-wide entanglement structures — the relationship between these metrics and actual computational utility remains poorly understood. The fact that models without entangling gates can perform comparable to those with entanglement in QCCNNs, while the opposite trend appears in the quantum neural networks of the first methodology, suggests that entanglement requirements may be context-dependent and influenced by other architecture factors, such as the relative importance of classical versus quantum processing components. Given the availability of entanglement is one of the key resources separating quantum and classical methods, we strongly believe that improving the general understanding of the role of entanglement in quantum machine learning models is a crucial future research direction. Since a major difference between the two methodologies is the number of trainable parameters, we believe a good starting point for future work would be to test the usefulness of entanglement in quantum circuits with a fixed number of trainable parameters. Crucial but specific open questions are: (i) “which type of data structures benefit from entanglement?”, (ii) “how does the amount of classical processing in a hybrid model impact the use-

fulness of entanglement?” and (iii) “how to best quantify the entanglement in a quantum circuit and how to relate it to model performance?”. Regarding this last open question, many metrics can be considered, such as the structure of the entangling gates, their type, their number, and the per-gate or total entangling power. Moreover, looking at state entanglement metrics could prove more insightful than gate-level metrics, since they not only take into account the circuit unitary, but also the data being processed. This can be tackled by quantifying the full state entanglement as the initial (non-entangled) state propagates through the quantum circuit, giving rise to potentially complicated multi-partite entanglement before measurement. This can reveal whether the entangling capabilities of any gates are actually used to create entanglement in the states generated with each specific data set. Unfortunately, this analysis is computationally very expensive, which is why we did not include it in this study.

Our cross-data set analysis reveals that quantum-model transferability is limited, with performance possibly dependent on data-separability characteristics. Models performing well on linearly-separable data showed mediocre performance on the more complex, non-linearly separable industrial images. While there seems to be a correlation between model architecture and class separability, further research is needed to confirm this hypothesis. This suggests that, despite the universal approximation capabilities theoretically attributed to quantum models, custom architecture design remains necessary for optimal performance on specific data sets.

We approached this study with fairness considerations in both directions: restricting the parameter count of classical models to match quantum models, while limiting quantum model size to ensure compatibility with near-term quantum devices and classical simulability. Despite these constraints, our findings provide valuable insights into the current state of quantum machine learning for industrial image classification. The absence of performance advantage, combined with our systematic hyperparameter optimization analysis, illustrates the significant gap between theoretical quantum advantage propositions and practical implementations.

The question of whether one model outperforms another also strongly depends on the performance metric. Here, we exclusively use the classification accuracy on the validation data set, although other metrics such as convergence

speed or training time could, in principle, be employed. However, for the latter, it would be difficult to make a tangible statement without running all quantum circuits on actual quantum hardware — instead of simulating them — and factoring in data loading and circuit execution times as well as their frequent repetition until enough statistics would be gathered. Hence, until sufficiently potent quantum hardware is available, it is difficult to judge the practical potential of quantum-machine-learning methods, since, up to then, either a classical preprocessing of data or a restriction of quantum resources is required — both heavily impacting the conclusions one may draw from any results. Nevertheless, our comprehensive hyperparameter study provides a methodological framework and empirical baseline for future quantum-machine-learning research focused on realistic industrial applications, offering crucial insights into the current limitations and potential directions for advancement in this rapidly evolving field.

ACKNOWLEDGMENTS

This work was supported by the Federal Ministry for Economic Affairs and Climate Action (Bundesministerium für Wirtschaft und Klimaschutz) within the project “AutoQML“ and project numbers 01MQ22002A and 01MQ22002B.

CONTRIBUTION STATEMENT

D.B.: Conceptualization, Methodology, Software, Validation, Formal analysis, Investigation, Writing, Visualization. **J.B.:** Conceptualization, Methodology, Software, Validation, Formal analysis, Investigation, Writing, Visualization. **C.T.:** Funding Acquisition, Supervision. **F.S.:** Conceptualization, Supervision, Funding Acquisition.

DATA AVAILABILITY

The data used in this study is available upon reasonable request.

COMPETING INTERESTS

The authors declare no competing interests.

-
- [1] M. Schuld, I. Sinayskiy, and F. Petruccione, An introduction to quantum machine learning, *Contemp. Phys.* **56**, 172 (2014).
 - [2] J. Biamonte, P. Wittek, N. Pancotti, P. Rebentrost, N. Wiebe, and S. Lloyd, Quantum machine learning, *Nature* **549**, 195–202 (2017).
 - [3] S. Lloyd, M. Mohseni, and P. Rebentrost, Quantum algorithms for supervised and unsupervised machine learning, *arXiv:1307.0411* (2013).
 - [4] P. Rebentrost, M. Mohseni, and S. Lloyd, Quantum support vector machine for big data classification, *Phys. Rev. Lett.* **113**, 130503 (2014).

- [5] K. Mitarai, M. Negoro, M. Kitagawa, and K. Fujii, Quantum circuit learning, *Phys. Rev. A* **98**, 032309 (2018).
- [6] M. Schuld, A. Bocharov, K. M. Svore, and N. Wiebe, Circuit-centric quantum classifiers, *Phys. Rev. A* **101**, 032308 (2020).
- [7] Y. Du, M.-H. Hsieh, T. Liu, and D. Tao, Expressive power of parametrized quantum circuits, *Phys. Rev. Res.* **2**, 033125 (2020).
- [8] H.-Y. Huang, M. Broughton, M. Mohseni, R. Babbush, S. Boixo, H. Neven, and J. R. McClean, Power of data in quantum machine learning, *Nat. Commun.* **12**, 2631 (2021).
- [9] H.-Y. Huang, R. Kueng, and J. Preskill, Information-theoretic bounds on quantum advantage in machine learning, *Phys. Rev. Lett.* **126**, 190505 (2021).
- [10] S. Jerbi, C. Gyurik, S. C. Marshall, R. Molteni, and V. Dunjko, Shadows of quantum machine learning, *Nat. Commun.* **15**, 5676 (2024).
- [11] Y. Liu, S. Arunachalam, and K. Temme, A rigorous and robust quantum speed-up in supervised machine learning, *Nat. Phys.* **17**, 1013–1017 (2021).
- [12] D. Ristè, M. P. da Silva, C. A. Ryan, A. W. Cross, A. D. Córcoles, J. A. Smolin, J. M. Gambetta, J. M. Chow, and B. R. Johnson, Demonstration of quantum advantage in machine learning, *npj Quantum Inf.* **3**, 16 (2017).
- [13] H.-Y. Huang, M. Broughton, J. Cotler, S. Chen, J. Li, M. Mohseni, H. Neven, R. Babbush, R. Kueng, J. Preskill, and J. R. McClean, Quantum advantage in learning from experiments, *Science* **376**, 1182–1186 (2022).
- [14] H. Xu, T. Xiao, J. Huang, M. He, J. Fan, and G. Zeng, Toward heisenberg limit without critical slowing down via quantum reinforcement learning, *Phys. Rev. Lett.* **134**, 120803 (2025).
- [15] M. Schuld and N. Killoran, Is quantum advantage the right goal for quantum machine learning?, *PRX Quantum* **3**, 030101 (2022).
- [16] J. Bowles, S. Ahmed, and M. Schuld, Better than classical? the subtle art of benchmarking quantum machine learning models, [arXiv:2403.07059](https://arxiv.org/abs/2403.07059) (2024).
- [17] M. Cerezo, M. Larocca, D. García-Martín, N. L. Diaz, P. Braccia, E. Fontana, M. S. Rudolph, P. Bermejo, A. Ijaz, S. Thanasilp, E. R. Anschuetz, and Z. Holmes, Does provable absence of barren plateaus imply classical simulability? or, why we need to rethink variational quantum computing, [arXiv:2312.09121](https://arxiv.org/abs/2312.09121) (2024).
- [18] P. Bermejo, P. Braccia, M. S. Rudolph, Z. Holmes, L. Cincio, and M. Cerezo, Quantum convolutional neural networks are (effectively) classically simulable, [arXiv:2408.12739](https://arxiv.org/abs/2408.12739) (2024).
- [19] A. Angrisani, A. Schmidhuber, M. S. Rudolph, M. Cerezo, Z. Holmes, and H.-Y. Huang, Classically estimating observables of noiseless quantum circuits, [arXiv:2409.01706](https://arxiv.org/abs/2409.01706) (2024).
- [20] L. Deng, The MNIST database of handwritten digit images for machine learning research, *IEEE Signal Processing Magazine* **29**, 141 (2012).
- [21] M. Henderson, S. Shakya, S. Pradhan, and T. Cook, Quantum convolutional neural networks: Powering image recognition with quantum circuits, [arXiv:1904.04767](https://arxiv.org/abs/1904.04767) (2019).
- [22] A. Pérez-Salinas, A. Cervera-Lierta, E. Gil-Fuster, and J. I. Latorre, Data re-uploading for a universal quantum classifier, *Quantum* **4**, 226 (2020).
- [23] M. Schuld, R. Sweke, and J. J. Meyer, Effect of data encoding on the expressive power of variational quantum-machine-learning models, *Phys. Rev. A* **103**, 032430 (2021).
- [24] S. Lloyd, M. Schuld, A. Ijaz, J. Izaac, and N. Killoran, Quantum embeddings for machine learning, [arXiv:2001.03622](https://arxiv.org/abs/2001.03622) (2020).
- [25] M. Schuld, M. Fingerhuth, and F. Petruccione, Implementing a distance-based classifier with a quantum interference circuit, *EPL* **119**, 60002 (2017).
- [26] J. R. McClean, S. Boixo, V. N. Smelyanskiy, R. Babbush, and H. Neven, Barren plateaus in quantum neural network training landscapes, *Nat. Commun.* **9**, 4812 (2018).
- [27] E. Grant, L. Wossnig, M. Ostaszewski, and M. Benedetti, An initialization strategy for addressing barren plateaus in parametrized quantum circuits, *Quantum* **3**, 214 (2019).
- [28] M. Cerezo, A. Sone, T. Volkoff, L. Cincio, and P. J. Coles, Cost function dependent barren plateaus in shallow parametrized quantum circuits, *Nat. Commun.* **12**, 1791 (2021).
- [29] T. L. Patti, K. Najafi, X. Gao, and S. F. Yelin, Entanglement devised barren plateau mitigation, *Phys. Rev. Res.* **3**, 033090 (2021).
- [30] A. Deshpande, M. Hinsche, S. Najafi, K. Sharma, R. Sweke, and C. Zoufal, Dynamic parameterized quantum circuits: expressive and barren-plateau free, [arXiv:2411.05760](https://arxiv.org/abs/2411.05760) (2024).
- [31] I. Cong, S. Choi, and M. D. Lukin, Quantum convolutional neural networks, *Nat. Phys.* **15**, 1273–1278 (2019).
- [32] A. Pesah, M. Cerezo, S. Wang, T. Volkoff, A. T. Sornborger, and P. J. Coles, Absence of barren plateaus in quantum convolutional neural networks, *Phys. Rev. X* **11**, 041011 (2021).
- [33] M. Cerezo, A. Arrasmith, R. Babbush, S. C. Benjamin, S. Endo, K. Fujii, J. R. McClean, K. Mitarai, X. Yuan, L. Cincio, and P. J. Coles, Variational quantum algorithms, *Nat. Rev. Phys.* **3**, 625–644 (2021).
- [34] F. Struckmeier and F. Puente León, Nesting in the sheet metal industry: dealing with constraints of flatbed laser-cutting machines, *Procedia Manuf.* **29**, 575 (2019).
- [35] F. Struckmeier, P. Blättner, and F. Puente León, Methods for the localization of supporting slats of laser cutting machines in single images, in *Forum Bildverarbeitung 2020* (KIT Scientific Publishing, 2020) pp. 197–209.
- [36] A. F. Agarap, Deep learning using rectified linear units (ReLU), [arXiv:1803.08375](https://arxiv.org/abs/1803.08375) (2018).
- [37] D. A. Kreplin, M. Willmann, J. Schnabel, F. Rapp, M. Hagelüken, and M. Roth, sQUlearn – a python library for quantum machine learning, [arXiv:2311.08990](https://arxiv.org/abs/2311.08990) (2023).
- [38] M. Abadi, A. Agarwal, P. Barham, E. Brevdo, Z. Chen, C. Citro, G. S. Corrado, A. Davis, J. Dean, M. Devin, S. Ghemawat, I. Goodfellow, A. Harp, G. Irving, M. Isard, Y. Jia, R. Jozefowicz, L. Kaiser, M. Kudlur, J. Levenberg, D. Mané, R. Monga, S. Moore, D. Murray, C. Olah, M. Schuster, J. Shlens, B. Steiner, I. Sutskever, K. Talwar, P. Tucker, V. Vanhoucke, V. Vasudevan, F. Viégas, O. Vinyals, P. Warden, M. Wattenberg, M. Wicke, Y. Yu, and X. Zheng, *TensorFlow: Large-scale machine learning on heterogeneous systems* (2015), software available from tensorflow.org.
- [39] D. P. Kingma and J. Ba, Adam: A method for stochastic optimization, [arXiv:1412.6980](https://arxiv.org/abs/1412.6980) (2014).
- [40] T. Hubregtsen, D. Wierichs, E. Gil-Fuster, P.-J. H. S. Derks, P. K. Faehrmann, and J. J. Meyer, Training quantum embedding kernels on near-term quantum computers,

- Phys. Rev. A* **106**, 042431 (2022).
- [41] B. Jaderberg, A. A. Gentile, Y. A. Berrada, E. Shishenina, and V. E. Elfving, Let quantum neural networks choose their own frequencies, *Phys. Rev. A* **109**, 042421 (2024).
- [42] J. Berberich, D. Fink, D. Pranjic, C. Tutschku, and C. Holm, Training robust and generalizable quantum models, *Phys. Rev. Res.* **6**, 043326 (2024).
- [43] E. Grant, M. Benedetti, S. Cao, A. Hallam, J. Lockhart, V. Stojevic, A. G. Green, and S. Severini, Hierarchical quantum classifiers, *npj Quantum Inf.* **4**, 65 (2018).
- [44] S. Cao, L. Wossnig, B. Vlastakis, P. Leek, and E. Grant, Cost-function embedding and dataset encoding for machine learning with parametrized quantum circuits, *Phys. Rev. A* **101**, 052309 (2020).
- [45] A. Matic, M. Monnet, J. M. Lorenz, B. Schachtner, and T. Messerer, Quantum-classical convolutional neural networks in radiological image classification, in *2022 IEEE International Conference on Quantum Computing and Engineering (QCE)* (2022) pp. 56–66.
- [46] T. Hur, I. F. Araujo, and D. K. Park, Neural quantum embedding: Pushing the limits of quantum supervised learning, *Phys. Rev. A* **110**, 022411 (2024).
- [47] K. Gili, G. Alonso, and M. Schuld, An inductive bias from quantum mechanics: learning order effects with non-commuting measurements, *Quantum Mach. Intell.* **6**, 67 (2024).
- [48] J. Bowles, V. J. Wright, M. Farkas, N. Killoran, and M. Schuld, *Contextuality and inductive bias in quantum machine learning* (2023), arXiv:2302.01365 [quant-ph].
- [49] I. Kerenidis and A. Luongo, Classification of the MNIST data set with quantum slow feature analysis, *Phys. Rev. A* **101**, 062327 (2020).
- [50] A. Senokosov, A. Sedykh, A. Sagingalieva, B. Kyriacou, and A. Melnikov, Quantum machine learning for image classification, *Mach. Learn.: Sci. Technol.* **5**, 015040 (2024).
- [51] J. Pointing, Do quantum neural networks have simplicity bias?, arXiv:2407.03266 (2024).
- [52] D. A. Kreplin and M. Roth, Reduction of finite sampling noise in quantum neural networks, *Quantum* **8**, 1385 (2024).
- [53] E. Peters, J. Caldeira, A. Ho, S. Leichenauer, M. Mohseni, H. Neven, P. Spentzouris, D. Strain, and G. N. Perdue, Machine learning of high dimensional data on a noisy quantum processor, *npj Quantum Inf.* **7**, 161 (2021).
- [54] B. Kraus and J. I. Cirac, Optimal creation of entanglement using a two-qubit gate, *Phys. Rev. A* **63**, 062309 (2001).
- [55] Y. Ji, X. Chen, I. Polian, and Y. Ban, Algorithm-oriented qubit mapping for variational quantum algorithms, *Phys. Rev. Appl.* **23**, 034022 (2025).